A COMPARISON OF X-BAND POLARIZATION PARAMETERS WITH IN-SITU MICROPHYSICAL MEASUREMENTS IN THE COMMA HEAD OF TWO WINTER CYCLONES

BY

JOSEPH A FINLON

THESIS

Submitted in partial fulfillment of the requirements
for the degree of Master of Science in Atmospheric Sciences
in the Graduate College of the
University of Illinois at Urbana-Champaign, 2015

Urbana, Illinois

Advisers:

Professor Robert Rauber
Professor Greg McFarquhar

ABSTRACT

Since the advent of dual-polarization radar, methods of classifying hydrometeors by type from measured polarization variables have been developed. However, the deterministic approach of existing hydrometeor classification algorithms of assigning only one dominant habit to each volume does not properly consider the distribution of habits present in that volume. During the Profiling of Winter Storms (PLOWS) field campaign the NSF/NCAR C-130 aircraft, equipped with in-situ microphysical probes, made multiple passes through the comma head of two cyclones as the Mobile Alabama X-band (MAX) dual-polarization radar performed range-height indicator scans in the same plane as the C-130 flight track. On 14-15 February and 21-22 February 2010, 579 and 202 coincident data points, respectively, were identified when the plane was within 10 s ($\sim$1 km) of a radar gate. Using the axis ratio (α), sphericity (β), maximum dimension D, and projected area A of the in-situ imaged crystals, the habit of each particle was identified. For all particles that occurred for times within different binned intervals of radar reflectivity (Z_{HH}) and of differential reflectivity (Z_{DR}), the reflectivity-weighted contribution of each habit, and the frequency distributions of α and β were determined. Habits with less circular shapes (bullet rosettes and aggregates) had greater contributions to the reflectivity compared to other habits when $Z_{HH} > 7$ dBZ and $Z_{DR} > 2$ dB. The presence of bullet rosettes and aggregates for similar Z_{HH} and Z_{DR} supports previous studies that bullet rosettes are the favored crystal species for aggregate formation. While irregular particles made up 40% of the observed shapes, only 55% of the Z_{HH}-Z_{DR} bins had irregular particles contribute over 40% of the reflectivity. Additionally, over 88% of the bins did not have a single habit contribute over 75% to the reflectivity. These findings show the general lack of dominance of a given habit for a particular Z_{HH} and Z_{DR}, and suggest that determining the probability of specific habits in radar volumes may be more suitable than the deterministic methods currently used.

This work is dedicated to my loving mother, Dawn, whose support and encouragement have given me the motivation to persevere both professionally and personally. Your memory will live on forever.

Acknowledgements

The operational, technical, and scientific support provided by NCAR's Earth Observing Laboratory, particularly Alan Schanot and the Research Aviation Facility staff for their efforts with the C-130, and the staff of the University of Alabama at Huntsville Severe Weather Institute and Radar & Lightning Laboratories facility for their support of the MAX radar deployment, are acknowledged. We thank Major Donald K. Carpenter and the U.S. Air Force Peoria National Guard for housing the C-130 during the project. The composite radar analyses in Fig. 8 were provided by the Iowa Environmental Mesonet maintained by the Iowa State University Department of Agronomy. This work was funded under National Science Foundation Grants ATM-0833828 and AGS-1247404 to the University of Illinois.

Table of Contents

1. Introduction

Particle identification using radars with dual-polarization capability has been investigated for several decades. Seliga and Bringi (1976) first interpreted measurements of radar reflectivity factor at horizontal polarization (Z_{HH}) and differential reflectivity (Z_{DR}) using theoretical calculations of the electromagnetic scattering by spheroids (Gans 1912) to relate the sizes and shapes of raindrops to rainfall rate. Subsequently, Hall et al. (1980), Aydin et al. (1986), and Bringi et al. (1986) attempted to interpret hydrometeor type using dual-polarization techniques to distinguish between ice (primarily in the form of hail) and water in cloud.

Much research has been done using polarization variables to characterize ice and water hydrometeor species. Hall et al. (1984) systematically identified classes of hydrometeors (wet and dry hail, wet and dry snow, high and low density ice, drizzle, and rain) as well as nonmeteorological targets such as ground clutter and insects, whereas Bringi et al. (1986) used scattering simulations and measurements of Z_{HH}, Z_{DR}, dual-frequency ratio, and linear depolarization ratio (LDR) in convective storms to detect hail.

Following these earlier efforts, numerous studies have applied a statistical approach to determine the dominant particle type within a radar sample volume. The Boolean decision tree method was originally used to classify hydrometeor types based on predefined boundaries of radar measurements such as Z_{HH} and Z_{DR} (Höller et al. 1994; El-Magd et al. 2000; Schuur et al. 2012). The use of static boundaries for Z_{HH} and Z_{DR}, however, may lead to misclassification given that expected values of Z_{HH} and Z_{DR} are not mutually exclusive for different hydrometeor types, and measurement errors in the data may wrongly associate a variable's value with a particular hydrometeor type (Lim et al. 2005; Al-Sakka et al. 2013). As a result, the fuzzy logic technique has been more widely implemented in classification algorithms (e.g., Straka and Zrnić 1993; Vivekanandan et al. 1999; Zrnić et al. 2000, 2001; Dolan and Rutledge 2009; Park et al. 2009; Lim et al. 2013; Thompson et al. 2014; Picca et al. 2014). With fuzzy logic, the use of probability distribution functions for polarimetric

variables such as Z_{HH}, Z_{DR}, LDR, specific differential phase (K_{DP}), and copolar cross-correlation coefficient (ρ_{HV}), in addition to bright band location and temperature for each hydrometeor type, permit decisions on dominant hydrometeor type despite data that overlaps hydrometeor types or are contaminated by noise (Liu and Chandrasekar 2000). Most recently, Bechini and Chandrasekar (2015) and Wen et al. (2015) improved the use of fuzzy logic algorithms by incorporating a K-means clustering technique that imposes additional spatial contiguity constraints for particular hydrometeor classes.

The hydrometeor classification algorithm implemented across the WSR-88D network today uses Z, Z_{DR}, ρ_{HV}, K_{DP}, and parameters characterizing fluctuations of the Z and differential phase (ϕ_{DP}) fields along a radial to distinguish between 10 different hydrometeor classes (big drops, rain, heavy rain, rain/hail, dry snow, wet snow, crystals, graupel, biological scatterers, and ground clutter) for each radar sample volume (Park et al. 2009). In its current state, the membership functions associated with this hydrometeor classification algorithm are largely based on theoretical scattering simulations of particles (Al-Sakka et al. 2013) and a rather limited understanding of how hydrometeors are manifested in the polarization variables. There has been insufficient verification of these algorithms using in-situ data. While some studies have used coincident datasets of in-situ observations of hydrometeor type along with radar polarization variables (Liu and Chandrasekar 2000; Lim et al. 2005; Plummer et al. 2010), aircraft in-situ verification of hydrometeor classification is relatively rare.

Given the frequent nature of overlapping polarimetric properties for different particle habits, the probability distribution functions may at times be close among several hydrometeor types (Tang et al. 2013). For this reason, assigning a single hydrometeor species to a particular radar pixel may not be the most appropriate technique. Plummer et al. (2010) used a different approach by evaluating the *probability* that a particular phase (supercooled water versus ice) was occurring in the radar volume. This probabilistic approach may also be suitable for ice particle habit identification given the frequent inhomogeneity of hydrometeors in a given volume, but has yet to be tested.

The goal of this study is to relate in-situ measurements of ice particle habits, bulk cloud properties, and measurements of particle morphology to Z_{HH} and Z_{DR} measured by an X-band ground-based dual-polarization radar during the Profiling of Winter Storms (PLOWS) field campaign. A probabilistic approach, similar to that by Plummer et al. (2010), is used to establish possible habits of ice particles and their quantities within a radar sample volume. Further, it is explored whether it is more appropriate to use a deterministic approach to assign one habit to each radar pixel or a probabilistic approach that assigns multiple habits simultaneously to the same pixel. Two mass estimation approaches are finally explored to evaluate the reflectivity-weighted contributions for each particle habit as it relates to Z_{HH} and Z_{DR}. A description of the radar and aircraft instrumentation processing techniques is provided in Sec. 2. A brief synoptic overview of the two winter cyclones sampled is provided in Sec. 3. Results of individual particle microphysical properties are presented in Sec. 4, and findings of habit contributions as they relate to the radar measured variables are given in Sec. 5. A summary and major conclusions are provided in Sec. 6.

2. Data & Methodology

The data in this study were collected within the 14-15 and 21-22 February 2010 winter cyclones sampled during the 2009/10 Profiling of Winter Storms (PLOWS) field campaign. A description of PLOWS can be found in Rauber et al. (2014). For this study, data from the University of Alabama-Huntsville (UAH) Mobile Alabama X-band (MAX) dual-polarization radar and in-situ probes aboard the National Science Foundation/National Center for Atmospheric Research (NSF/NCAR) C-130 aircraft are used.

a. Identification of Coincident Aircraft/Radar Data

During PLOWS, an attempt was made to place the C-130 aircraft in the same plane as range-height indicator (RHI) scans from the ground-based MAX radar. This was done continuously for 7 hours on 14-15 February and 2 hours on 21-22 February as the storms evolved. The azimuth angle of the MAX radar was flipped 180^o to match the aircraft's heading as it passed back and forth directly over the radar site. The aircraft made vertically-stacked passes to obtain microphysical data at different altitudes below cloud top.

The aircraft was defined to be within the domain of the MAX radar when the aircraft was within 100 km of the radar and within 2 degrees of the RHI plane. Each coincident observation encompasses several seconds of aircraft microphysical data and radar gates in the vicinity of the aircraft's location as outlined below. A total of 576 coincident observations (343 in cloud) were collected during the 14-15 February cyclone, and 202 (142 in cloud) during the 21-22 February cyclone. Table 1 lists the number of coincident observations in the cloud for each of the constant altitude flight legs flown and the average temperature of each.

Specific criteria were developed to determine the temporal and spatial limits for when the microphysical and radar measurements were collocated. Example RHI scans of Z_{HH} (in dBZ) with the plane's collocated position are shown in Fig. 1, with the inset showing

gates (including gates contaminated by aircraft echo) that are considered coincident given the following criteria. Particle data within five seconds of flight from the collocated point (corresponding to $\sim$ 0.5 km on either side given an aircraft speed of 100 m s^{-1}), and radar gates between 250 and 500 m on either side of the point with a maximum altitude difference of no more than 25 m from the aircraft altitude were used for the comparison. In order to avoid contamination of the radar signal by the aircraft, radar gates within 250 m of the aircraft location were ignored irrespective of whether the aircraft directly intersected the radar beam. Data associated with a coincident point were verified to have no contamination by analyzing the variance in reflectivity values from all applicable gates. The Z_{HH} and Z_{DR} measurements were then averaged for all radar data collocated within 50 m vertically and 250-500 m horizontally on either side of the coincident point. A sensitivity study showed that averaging over greater horizontal (between 250 m and 1 km) and vertical (100 m) distances yielded an average difference of 12% in the mean Z_{HH} for gates associated with the coincident point, while averaging over smaller horizontal (between 250 and 400 m) and vertical (50 m) distances only yielded an average difference of 5%. Direct comparison of particle information (habit, size distribution, axis ratio, median mass diameter D_{mm}) with coincident radar data was thus possible using this approach.

b. In-situ Measurements

Particle imagery from the two-dimensional cloud (2D-C) and precipitation (2D-P) optical array probes (OAPs) were used to derive microphysical quantities, including single particle axis ratio (α), sphericity (β), mass (m), and habit, and measures of distributions of particles such as the number distribution function N(D), median mass diameter (D_{mm}), and ice water content (IWC).

Data from the OAPs were processed using algorithms that were originally developed at NCAR and thereafter modified at the University of Illinois. Jackson et al. (2014) describes the processing techniques, including criteria to accept and reject particles. Processing details

specific to the PLOWS dataset can be found in Plummer et al. (2014, 2015). The 2D-C was used to characterize N(D) for $500 < \mathrm{D} < 2100$ μm and the 2D-P for $2100 < \mathrm{D} < 9600$ μm. Following Heymsfield and Baumgardner (1985) and Field (1999), only particles with a center of mass within the OAP's field of view were considered to avoid classification where there was too much uncertainty in particle shape. Particles smaller than 500 μm were not used in the analysis because of uncertainties due to particle shattering (Korolev et al. 2011, 2014; Jackson et al. 2014), and, in any event, do not make substantial contributions to Z_{HH}, which is dominated by larger particles.

Particle axis ratio for this study was defined by

$$\alpha = \frac{L_H}{L_V}, \tag{1}$$

where L_H is the particle length along the time dimension determined by the aircraft speed and the duration that a particle shadows the probe's photodiodes, and L_V is the number of diodes shadowed multiplied by the probe resolution as illustrated in Fig. 2. The axis ratio is useful for the interpretation of Z_{DR} because particle shape and orientation influences the radar backscatter energy at horizontal and vertical polarizations. Particle sphericity (β, McFarquhar et al. 2005) for particles entirely within the OAP's field of view was defined by

$$\beta = \frac{\sqrt{A}}{P}, \tag{2}$$

where the cross-sectional area A is directly measured by the probe and P is the perimeter determined as the sum of all pixels within one diode width of the edge of the particle multiplied by the diode resolution (Fig. 2). The β represents the roundness of a particle imaged by an OAP regardless of orientation, with higher values denoting more circular particles. The reflectivity-weighted average of α and β were computed from a population of ice particles as

$$\bar{\alpha} = \frac{\sum_j Z_j \alpha_j}{\sum_j Z_j} \tag{3}$$

and

$$\bar{\beta} = \frac{\sum_j Z_j \beta_j}{\sum_j Z_j}, \tag{4}$$

where Z_j is the reflectivity of an individual particle and the summation over j denotes summation over all particles within a sample population.

Particle habits were identified using the classification scheme of Holroyd (1987), modified to classify particles into nine categories: aggregate, bullet rosette, hexagonal, graupel, spherical, linear, oriented, irregular, and tiny. Given the coarser resolution of the 2D-P probe and its inability to resolve more intricate particle features, particle shape information was only derived using the 2D-C data. The reflectivity distributions computed below show that these particles measured by the 2D-C with 500 μm $<$ D $<$ 2100 μm contributed 94% on average to the total reflectivity, justifying this approach. A series of decisions regarding the particle's size, perimeter, axis ratio, orientation, and number of unshadowed diodes within the particle boundaries were used to determine habit. Extensive visual analysis of crystals classified as dendrites showed that they are typically a collection of columnar crystals rather than branched in nature. This visual difference not captured in the algorithm, together with the fact that temperatures in situ were generally colder than that typical for dendritic growth (Table 1), justified classifying those particles as bullet rosettes (Fig. 3). Particles classified as graupel (Fig. 3) may be more accurately identified as ice pellets given their size and overall appearance. Since particles smaller than 500 μm were eliminated to avoid shattered artifacts, very few particles classified as "tiny" remained and this habit category was ignored in subsequent analyses. Oriented columns were classified as being positioned 30-60° from the vertical axis. Although oriented crystals may result from turbulence around the probe inlets and disturbed flow around the aircraft fuselage (King 1985, 1986; Hogan et al. 2012) rather than strong electrostatic fields within the cloud (Griffin et al. 2014), they are nonetheless treated separately from other columns in the analysis.

Particle mass is needed for calculating the radar reflectivity factor from the size and

habit distributions. Two approaches were used to estimate m. The first estimates m from the projected area A of each particle as originally applied to the PLOWS data by Plummer et al. (2014, 2015) following Baker and Lawson (2006), hereafter BL06. The second uses mass-diameter (m-D) relationships specific to each habit as outlined in McFarquhar et al. (2002) (hereafter M02), and subsequently applied by Jackson et al. (2014). Fig. 4 shows the mass of an individual particle of length D following BL06 for different area ratios (A_r, defined as the ratio of the particle's projected area to the area of a circumscribed circle) and for different habits. It is seen that particles with the same diameter can have substantially different masses, with particles of D at 500 μm (2000 μm), for example, having masses vary between 0.002 (0.055) mg and 0.012 (0.541) mg depending on the assumed habit or area ratio. Analysis herein will compare both approaches to examine differences in the results.

c. Mobile Alabama X-band (MAX) Radar

The MAX radar, transmitting at a wavelength of 3.17 cm (9450 MHz), retrieved polarization measurements of Z_{HH}, Z_{DR}, K_{DP}, and ρ_{HV}, as well as radial velocity and spectrum width. The high spatial variation of K_{DP} at X band and low Z_{HH} in snow mentioned by Goddard et al. (1994), Bringi and Chandrasekar (2001), and Ryzhkov et al. (2005), in addition to high K_{DP} variance from neighboring radar gates during PLOWS, prompted the exclusion of K_{DP} in this study. Further details regarding the MAX radar can be found in Mullins and Knupp (2009) and Knupp et al. (2013). Processing techniques specific to the PLOWS data are described below.

The RVP8 signal processor used in the MAX radar during PLOWS produces an error in the recorded elevation angle of RHI scans when the radar scans downward. This artifact is evident in animations between consecutive RHIs of the same azimuth, with a visible jump occurring between the scans. The elevation angle for upward RHI scans was determined correct by comparing the altitude and position of aircraft echoes on radar with the GPS location of the aircraft. To correct the elevation angle for the downward scans, the reflectivity

for all RHIs at the same azimuth angle was first interpolated onto a Cartesian grid with a horizontal resolution of 100 m and a vertical resolution of 50 m using an inverse distance weighting function. A series of different elevation angle adjustments ranging from -0.15 to 0.15° about the recorded angle were then tested for the downward RHIs by interpolating the reflectivity of each elevation angle adjustment to a grid. For pixels where the radar signal was less sensitive to noise (within 30 km of the radar and 3 km of the ground), the sum of squared differences between an upward RHI and each elevation angle adjustment for the subsequent downward RHI of the same azimuth angle was computed as

$$\sum_{i,j}(Z_{up,i,j} - Z_{down,i,j})^2, \tag{5}$$

where $Z_{up,i,j}$ is the reflectivity of the upward RHI scan at grid point (i, j) and $Z_{down,i,j}$ is the reflectivity of the downward RHI scan (in mm^6 m^{-3}) with the appropriate elevation angle adjustment at that point. The elevation angle adjustment of the downward RHI which minimized this value was then adopted. This process was repeated for each upward-downward RHI pair, with the majority of downward RHIs being adjusted by 0.05°. Adjustments were verified by comparing the altitude and position of aircraft echoes on adjusted downward RHI scans with the GPS location of the aircraft. The interpolated data were only used for determining the elevation angles; the radar data used in the remainder of this study are the recorded data as a function of range and elevation angle.

Z_{HH} and Z_{DR} are biased at X-band due to attenuation and differential attenuation, respectively, especially in regions of liquid precipitation. Increasingly sophisticated algorithms (e.g. Bringi et al. 1990; Delrieu et al. 2000; Testud et al. 2000; Bringi et al. 2001; Gorgucci and Chandrasekar 2005; Chandrasekar et al. 2006; Chang et al. 2014) are available for attenuation correction, with applications for rainfall estimation (Ryzhkov et al. 2014; Diederich et al. 2014a,b) and hydrometeor classification (Snyder et al. 2010).

The reliance of K_{DP} with the above algorithms combined with the omission of K_{DP} data for this study prompted use of the Park et al. (2005a) algorithm to correct for attenuation for points below the radar bright band. The bright band height (∼1 km above ground) for

the 21-22 February cyclone was determined for each RHI by computing the mean height of maximum Z_{HH} values for a series of radar beams along the RHI. No corrections to Z_{HH} and Z_{DR} were needed for the 14-15 February event given temperatures at all levels remained below 0°C and precipitation fell as snow.

d. Analysis of Coincident Datasets

The estimated reflectivity of each particle (Z_p) was calculated over the entire flight sampling period following the mass-area relationship of BL06 and habit dependent m-D relations. The per-particle reflectivity for times when the C-130 aircraft and MAX radar were coincident represents a subset of the entire flight sampling period. To remain consistent with the habit analysis within the 2D-C size range, only particles sampled by the 2D-C with 500 μm $< D <$ 2100 μm were considered. Fig. 5 shows the reflectivity distribution function $Z(D)$ of particles from a 10-second sample at 0701 UTC on 15 February when the Z_{HH} near the aircraft's location was above 20 dBZ. It is seen that the contribution to the reflectivity for $D >$ 2250 μm, namely particle sizes measured by the 2D-P, is $< 20\%$ despite sampling a more intense part of the cloud (a few minutes after the RHI shown in Fig. 1). $Z(D)$ for particles at larger sizes are an order of magnitude less than $Z(D)$ for size bins towards the high end of the 2D-C size range.

In order to relate the aircraft derived microphysical properties (Z_p, $\bar{\alpha}$, $\bar{\beta}$) to Z_{HH} and Z_{DR} measured by the radar, the in-situ derived properties were sorted into specific Z_{HH}-Z_{DR} bins following the approach of Plummer et al. (2010). Use of Z_{HH}-Z_{DR} binned intervals in their study permitted development of lookup tables that provided probability estimates of supercooled liquid water present in a cloud at given Z_{HH} and Z_{DR} measurements.

The domain used in this study encompassed -11 $< Z_{HH} <$ 15 dBZ and 0 $< Z_{DR} <$ 4 dB based on the distribution of the polarization variables measured for each event. Fig. 6 shows the distribution of Z_{HH} and Z_{DR} measurements for each event and the range of values used in the domain. Thirteen Z_{HH} and eight Z_{DR} bins (separated by 2.0 dBZ and 0.5

dB increments, respectively) were chosen to provide sufficient resolution to determine how microphysical properties change with Z_{HH} and Z_{DR} while maintaining sufficient data in each binned interval. The number of accepted particles sampled by the 2D-C for each event corresponding to a specific Z_{HH}-Z_{DR} bin is presented as the top number in Fig. 7, while the bottom set of numbers represents the aircraft sampling duration (in seconds).

3. Cyclone Events

The 14-15 and 21-22 February 2010 cyclones were chosen because of the extended duration that the aircraft sampled within the domain of the MAX radar. The first cyclone examined, an Alberta clipper-type cyclone, moved over the western Ohio River valley on 15 February 2010 as a shortwave originated from the Canadian Rockies. A 350-hPa jet streak was present at the time of the PLOWS operations (0200 to 1600 UTC), with the surface cyclone underneath its left exit region. The low pressure center traveled from northern Alberta to northern Kentucky over a three-day period, with its center located in western Kentucky at the time of the aircraft flight (Fig. 8a). At that time the minimum pressure was 1009 hPa with the comma head region extending from southwestern Missouri to eastern Illinois. The C-130 made repeated passes directly north of the cyclone between southern Illinois and southern Indiana (Table 1, Fig. 8a). Rosenow et al. (2014), Plummer et al. (2014), and Plummer et al. (2015) provide a more complete overview of the synoptic conditions, vertical velocity, and microphysical structure associated with the cyclone.

The second cyclone examined here, which originated over eastern New Mexico, developed as a weak 500-hPa shortwave, exited the Rocky Mountains, and then moved over the midwest Plains states. An area of surface low pressure developed from an inverted surface trough by 0000 UTC 21 February, with the comma head precipitation forming as the cyclone moved from eastern New Mexico to northwest Ohio over a two-day period. At the time of the C-130 flight, the surface cyclone had a minimum pressure of 1006 hPa in southeast Missouri, with the comma head region extending from eastern Kansas to central Illinois. The C-130 repeatedly flew along the track (Table 1, Fig. 8b) between northern and southern Illinois.

The two cyclones exhibited significant differences regarding their precipitation extent and thermodynamic structure. Temperatures at the surface (0 - 2°C) and aloft were warmer for the 21-22 February cyclone as evidenced by temperatures from flight legs of comparable altitude (Table 1) and the presence of a melting layer and a radar bright band (Fig. 1b). While maximum reflectivity values from the RHIs were comparable between both cyclones

(Fig. 1), the range of measured Z_{HH} at the aircraft's location (Fig. 6a) was notably greater for the 14-15 February case (-15 $< Z_{HH} <$ 15 dBZ) compared to the 21-22 February case (-15 $< Z_{HH} <$ 2.5 dBZ) due to a greater penetration depth below cloud top as the aircraft made vertically stacked passes (Fig. 1a). The range of Z_{DR} values at the aircraft's location (Fig. 6b) were found to be similar (-2 $< Z_{DR} <$ 4 dB) between the two cases.

4. Habit Microphysical Properties

Eight crystal habit categories of differing morphology were considered in the following analysis. Representative particles of these eight ice habits, as imaged by the 2D-C probe, are shown in Fig. 3. The remainder of this section discusses the distributions of Z_p, α, and β at points with coincident in-situ and radar data (hereafter called coincident points) for each habit, their representativeness to the entire sampling period, similarity between the 14-15 and 21-22 February cyclones, and sensitivity between the two mass estimation approaches.

a. Particle Representativeness of Coincident Points to the Entire Sampling Period

Fig. 9 shows distributions of Z_p for particles of each habit sampled at coincident points (red) and for the entire flight sampling period (blue) using mass estimations from the projected area in BL06. Statistics on the distribution mean (μ_c) and median ($\widetilde{x}_c$) from coincident periods, and the mean (μ_f) and median ($\widetilde{x}_f$) from the entire flight sampling period (in dBZ) for the 2 cyclones separately are also provided. The distributions for aggregates, for instance, are similar given the extent of overlap in the normalized frequencies and the small difference in the distribution mean (< 0.6 dBZ) and median (< 0.4 dBZ). Inspection of the distributions of Z_p for the other habits also suggests that the distributions of Z_p are similar for the entire sampling period and the coincident points.

To better quantify the similarity of Z_p for each habit between the entire sampling period and the coincident points, the Cohen's effect size d (Cohen 1988) was calculated. The effect size d represents the standardized mean difference between the two distributions, and is defined as

$$d = \frac{|\mu_c - \mu_f|}{\sqrt{\frac{\sigma_c^2 + \sigma_f^2}{2}}}, \tag{6}$$

where σ_c and σ_f are the distribution standard deviation for coincident particles and the entire flight sampling period, respectively, for the particular habit being considered. Cohen (1988) proposed that effect sizes under 0.2 suggest that differences between two distributions

are trivial. Calculated effect sizes (Table 2) indicate that while effect sizes of Z_p distributions for irregular crystals, bullet rosettes, and oriented columns during the 21-22 February 2010 cyclone are > 0.2, distributions of Z_p for all the other habits during the entire sampling period (figure not shown) are similar to those using the coincident points as evidenced by the Cohen's effect size. Effect sizes for the α and β distributions suggest that the differences between the entire sampling period and the coincident points are trivial given that values for all habits are < 0.2. Since the normalized frequency distributions of Z_p, α, and β are found to be similar between the entire sampling period and the coincident points, the remainder of the analysis in this paper only focuses on the coincident points.

b. Habit Distributions of Z_p, α, and β

The estimates of Z_p are dependent on how the particle masses are estimated. To examine the importance of these assumptions, Fig. 10 compares the distributions of Z_p for the coincident data points computed according to the BL06 and M02 computation techniques. The line for each distribution denotes the percentage of particles sampled during all coincident periods that have a Z_p less than or equal to the value along the abscissa. The histograms and cumulative frequency curves show that while many of the habits have a similar mean and median in the Z_p distributions between BL06 and the habit-specific relationships, notable differences do exist for bullet rosettes and graupel. The median Z_p when using habit-specific relationships is around 4 dBZ lower for bullet rosettes (Figs. 10c,d) and around 4.5 dBZ higher for graupel (Figs. 10i,j) compared to that estimated from BL06. These differences are explained by the typical particle mass with a D of 1 (2) mm yielding a mass of 0.078 (0.541) mg for graupel and 0.017 (0.081) mg for bullet rosettes compared to the mass derived from the projected area (BL06) being 0.037 (0.199) mg for an A_r of 0.5 (Fig. 4).

The distributions of Z_p are used to assess which habits contribute most to the reflectivity. Aggregates have the greatest Z_p values among the eight habits, with a median Z_p between -11.9 and -8.3 dBZ depending on the mass relationship used and cyclone sampled (Figs. 10e-

f). Irregular crystals, bullet rosettes, and graupel have the next highest values of Z_p. Median Z_p for irregular crystals and bullet rosettes range between -25 and -20 dBZ (Figs. 10a-d), while graupel typically has higher Z_p values of between -19 and -13 dBZ (Figs. 10i-j) given their greater density and resultant mass (Fig. 4). With median Z_p of around -30 dBZ or lower for hexagonal plates (Figs. 10g-h), linear (Figs. 10k-l) and oriented (Figs. 10m-n) columns, and spherical crystals (Figs. 10o-p), it is less likely that these habits yield meaningful contributions to the reflectivity. To determine the contributions that the different habits make to the observed reflectivity in a particular range gate, Z_{HH}, the reflectivities of individual particles and the concentrations of that size and shape particle must be known. Because the Z_p for certain habits (e.g., aggregates, irregular crystals, bullet rosettes, and graupel) can be orders of magnitude greater than the Z_p of other habits (e.g., hexagonal plates, columns, and spherical crystals), it is likely that only some particle habits make contributions to Z_{HH}. This is further investigated below.

In order to gain insight into particle shape as it relates to Z_{DR}, it is necessary to first understand how the distributions of α (Fig. 11) and β (Fig. 12) vary according to particle shape. In addition to the mean and median of α and β, statistics on the distribution standard deviation (σ_c) and skewness (Sk_c) are also shown for each habit in Fig. 11 and Fig. 12, respectively.

The α distributions indicate that bullet rosettes (Figs. 11c-d), aggregates (Figs. 11e-f), and linear columns (Figs. 11k-l) are most oblate with median α between 1.19 and 1.31. Larger skewness values between 1.03 and 2.11 for these habits also suggest that the horizontal dimensions for these habits can be noticeably greater than the vertical dimensions, for at least some particles, and thus cause higher Z_{DR} in clouds. Lower α values for hexagonal plates (Figs. 11g-h), graupel (Figs. 11i-j), and spherical particles (Figs. 11o-p) are the result of the ratio of the particle's horizontal and vertical dimensions being closer to unity. Given that the greatest value β can be for a spherical particle with D = 1 mm is 0.34, $\beta > 0.2$ for these habits (Figs. 12g-j,o-p) affirm their circular nature when projected onto a 2-D plane.

Small particle sizes for plates and spherical crystals, as described earlier, in conjunction with higher β values is consistent with a similar parameter used in Korolev and Isaac (2003). While α distributions for vertically-oriented columns have a median value between 0.72 and 0.75 (Figs. 11m-n), their shape (median β of 0.19) is similar to linear columns (median β of 0.18) given that μ_c, $\widetilde{x}_c$, σ_c, and Sk_c are nearly identical in the β distributions between both habits (Figs. 12k-n).

c. Particle Comparison Between Cyclones

With particle properties being examined for each habit rather than as a whole, the distributions of Z_p, α, and β are not expected to vary significantly between cyclones if the properties are truly habit dependent. In an effort to determine if the distributions of Z_p, α, and β determined for each of the habits varied between the 14-15 February and 21-22 February cyclones, the Cohen's effect size d was computed and the results are shown in Table 3. While differences between the distributions of Z_p, α, and β for many habits were smaller than 0.2 representing trivial differences, values greater than 0.2 are observed in the distributions of Z_p and β for aggregates, graupel, and spherical particles. This suggests the characteristics of these habits vary between cyclones. This is not surprising given that the density of graupel may vary depending on the temperature, fall velocity, and amount of riming while the characteristics of aggregates may vary depending on the compositional makeup of individual crystals. The temperatures were over 10°C higher for the 21-22 February 2010 cyclone at similar altitudes (Table 1) compared to the 14-15 February cyclone, and there were different penetration depths below cloud top within the comma head region on both days which thus probably accounts for differences in the microphysical characteristics for each habit. As a result, analysis of each habit's contribution as it relates to observed Z_{HH} and Z_{DR} is performed separately for each cyclone in Sec. 5.

d. Comparing In-situ Derived Reflectivity to Reflectivity from the MAX Radar

To further investigate the impact of the mass estimation approach on the calculated reflectivity, Fig. 13 shows the reflectivity computed by summing the contributions of all particles within 5 s (500 m) of the coincident radar gate ($Z_{ensemble}$) using the particle mass derived from the projected area and from the habit-dependent m-D relations as a function of the Z_{HH} measured by the MAX radar. The colored lines represent the mean $Z_{ensemble}$ value for all points within 2.5 dBZ wide Z_{HH} bins on the horizontal axis, with values above (below) the black (1:1) line indicating that derived reflectivities were greater than (less than) those measured by the MAX radar.

The mean difference in $Z_{ensemble}$ between the two approaches was 1.61 dBZ, with some coincident points yielding a maximum difference of 11.73 dBZ. Some of the points where Z_{HH} = -5 dBZ on 14-15 February corresponded to cases where graupel contributed 77% of the total reflectivity using the M02 approach compared to 41% using BL06, which partially explains the differences in $Z_{ensemble}$ due to a higher particle density used in the M02 approach for graupel. The RMSE between $Z_{ensemble}$ from each approach and Z_{HH} from the MAX radar varied for each cyclone, with the RMSE being 19% (5%) lower using the BL06 (M02) approach on 14-15 (21-22) February.

5. Habit Relationships to Z_{HH} and Z_{DR}

In this section, the contributions of the different habits to the total reflectivity is examined to allow for a more direct comparison with Z_{HH}.

a. Habit reflectivity contribution

For each Z_{HH}-Z_{DR} binned interval, the contribution of a habit to the ensemble reflectivity (Z^*) is defined as

$$Z^*(Z_{HH}, Z_{DR}, habit) = \frac{\sum_{particles} Z_p(Z_{HH}, Z_{DR}, habit)}{\sum_{habit} \sum_{particles} Z_p(Z_{HH}, Z_{DR}, habit)}, \quad (7)$$

with the denominator representing the sum of Z_p from all particles and habits sampled by the 2D-C for coincident points which is equivalent to $Z_{ensemble}$. Figs. 14 and 15 show Z^* for each habit computed using the mass relationship from BL06 and habit-specific m-D relationships, respectively. The sum of Z^* for all habits for a given Z_{HH}-Z_{DR} bin in each figure equals one.

The general distribution of Z^* for each habit in the Z_{HH}-Z_{DR} domain look similar between the mass estimation approaches aside from a couple exceptions. Contribution of bullet rosettes to the reflectivity approach 35% using the BL06 approach for $Z_{DR} > 2$ dB (Figs. 14c,d), and no greater than 20% using the habit-specific m-D relationship (Figs. 15c,d). Graupel, on the other hand, has Z^* values over 50% for 53% of the Z_{HH}-Z_{DR} bins for $Z_{DR} < 2.5$ dB on 14-15 February with the habit-specific m-D relationship, while only 13% of the bins have Z^* greater than 50% using the BL06 approach.

Overall, there are no large jumps in Z^* for any habit for small variations in either Z_{HH} or Z_{DR}. The bins encompassing $9 < Z_{HH} < 15$ dBZ and $2 < Z_{DR} < 3$ dB, for instance, have Z^* values that are consistent for a given habit. Bins that do have a noticeable jump in Z^*, like the bin containing $3 < Z_{HH} < 5$ dBZ and $1 < Z_{DR} < 1.5$ dB, can be explained by fewer than 100 particles sampled within the Z_{HH}-Z_{DR} bin (Fig. 7).

Some trends in Figs. 14 and Fig. 15 about which habits make the largest contributions to the reflectivity are evident. Irregularly-shaped crystals contribute at most 70 percent of the total reflectivity for bins where -11 $< Z_{HH} <$ 3 dBZ and 2 $< Z_{DR} <$ 4 dB (Figs. 14a,b; 15a,b). This is consistent with the results from Korolev et al. (1999) and Korolev et al. (2000) who indicated that roughly 80-95 percent of particles sampled were of "irregular" shape. On the other hand, Stoelinga et al. (2007) suggested that irregular crystals, as viewed under a microscope, may be less dominant than previously believed. Consistent with this, nearly all of the bins where $Z_{HH} > 3$ dBZ have irregular crystals contributing at most 40% to the reflectivity. Of the particles sampled by the 2D-C during the time frames shown in Figs. 14 and 15, 40% of the observed particles were of irregular shape (not shown), and 55% of the Z_{HH}-Z_{DR} bins had irregular particles contribute over 40% of the reflectivity. This means that during 45% of the time periods irregular crystals do not dominate the reflectivity field, as notable contributions come from other habits.

The reflectivity contributions of bullet rosettes (Figs. 14c,d; 15c,d) and aggregates (Figs. 14e,f; 15e,f) are generally larger at higher reflectivity ($Z_{HH} \gtrapprox 7$ dBZ) and differential reflectivity ($Z_{DR} \gtrapprox 2$ dB). To explain this result, their presence for $Z_{HH} > 7$ dBZ for the 14-15 February cyclone can be related to size distributions for each habit. As an example, Fig. 16 shows N(D) of each habit for the same 10-second interval as in Fig. 5, a period which experienced $Z_{ensemble} = 12.2$ dBZ. Bullet rosettes and aggregates have the greatest number concentrations for D > 1100 μm, with aggregates having concentrations 5-10 times that of the other habits for D > 1600 μm. Their contribution at higher Z_{DR} is explained by the median $\alpha = 1.19$ (1.31) and $\beta = 0.13$ (0.12) for bullet rosettes and aggregates, respectively (Figs. 11c-f;12c-f). Temperatures on 14-15 February were well below the optimal temperature of 0 °C for aggregation (Magono 1954), with -14 °C being the warmest temperature for a flight leg that day (Table 1). However, a greater presence of bullet rosettes for $Z_{HH} > 7$ dBZ and $Z_{DR} > 2$ dB may have enhanced the production of aggregates (e.g., Hobbs et al. 1974; Fujiyoshi and Wakahama 1985) that found that the crystalline structure of bullet rosettes and dendrites

promoted a greater likelihood of crystals sticking together.

Hexagonal plates are shown to contribute slightly more to the reflectivity when Z_{HH} at the aircraft's location is less than -5 dBZ (Figs. 14g,h; 15g,h). This is explained in the size distributions for hexagonal plates (Fig. 16), which indicate that number concentrations are greater for D < 1 mm.

The contribution to the reflectivity from graupel (Figs. 14i,j; 15i,j) fluctuates over small changes in Z_{HH} and Z_{DR}, particularly when $Z_{DR} < 2.5$ dB on 14-15 February. The sensitivity of Z^* is greater when using the habit-specific mass relationship (Fig. 15i) since the median Z_p = -13.3 dBZ (Figs. 10i,j) is larger than most habits and thus greatly affects Z^* depending on the number of graupel particles observed in a Z_{HH}-Z_{DR} bin. The fluctuations in Z^* are further explained based on the findings of Aydin and Seliga (1984) and Oue et al. (2015), who indicated that higher density graupel was found to exist over a wider range of Z_{DR}.

Linear, oriented, and spherical crystals make smaller contributions toward the total reflectivity because of their small sizes (Figs. 14k-p; 15k-p). The Z^* are less than 0.2 for these habits for nearly all Z_{HH} and Z_{DR} in the domain, with $Z^* < 0.05$ for spherical crystals over all measured Z_{HH} and Z_{DR}. While linear and oriented columns are observed for D as large as 1900 μm (Fig. 16), their concentrations are smaller than those of other habits and the median Z_p between -28.8 and -20.6 are lower than other habits (Figs. 10k-n) since their oblate shape, as evidenced by median β between 0.17 and 0.19 (Figs. 12k-n), yields a smaller radar backscatter cross section compared to habits of the same size that are more spherical (e.g., graupel). Furthermore, the observed concentrations of oriented columns are too small to contribute much to the reflectivity within the Z_{HH}-Z_{DR} domain used since their typical α values of less than 1 (Figs. 11m,n) correspond to negative Z_{DR} values.

b. Microphysics-polarization relationships

Trends in the variation of $\bar{\alpha}$ and $\bar{\beta}$ with Z_{HH} and Z_{DR} can be explained by the contributions that different habits make to the total reflectivity. Figs. 17 and 18 show $\bar{\alpha}$ and $\bar{\beta}$ for

each Z_{HH}-Z_{DR} bin where the reflectivity-weighted averages are performed over all particles in clouds with the appropriate Z_{HH} and Z_{DR} value. Because $\bar{\alpha}$ and $\bar{\beta}$ were weighted by the derived particle reflectivity, $\bar{\alpha}$ and $\bar{\beta}$ were calculated using the mass estimation approaches from BL06 and M02.

Values as high as 1.3 for $\bar{\alpha}$ (Figs. 17a,c) and as low as 0.09 for $\bar{\beta}$ (Figs. 18a,c), particularly with the 14-15 February cyclone, are observed for $Z_{HH} > 7$ dBZ and $Z_{DR} > 2$ dB. These extremes occur for the same set of Z_{HH} and Z_{DR} values that had larger contributions to the reflectivity from aggregates and bullet rosettes (Figs. 14c-f; 15c-f) whose larger median α between 1.9 and 1.31 (Figs. 11c-f) and smaller median β between 0.12 and 0.13 (Figs. 12c-f) have a greater effect on $\bar{\alpha}$ and $\bar{\beta}$ at these Z_{HH} and Z_{DR} values.

Values of $\bar{\alpha}$ ($\bar{\beta}$) are as low as (high as) 0.9 (0.25), particularly on 14-15 February, for Z_{HH} < 1 dBZ (Figs. 18a,c). Contributions to the reflectivity from hexagonal plates and graupel exceed 0.5 for 47% of the bins where $Z_{HH} < 1$ dBZ, which explains why $\bar{\alpha}$ ($\bar{\beta}$) is smaller (greater) in this region given median α (β) between 0.83 and 1.02 (0.21 and 0.23) for these habits (Figs. 11g-j; 12g-j).

While 40% of the bins within the Z_{HH}-Z_{DR} domain provide insight into the Z_{HH} and Z_{DR} values for which extremes of Z^*, $\bar{\alpha}$, and $\bar{\beta}$ are observed, the remaining 40% don't have a particular habit contribute over 50% to the total reflectivity (Fig. 14). The Z^* for each habit reiterates the inhomogeneity of crystal habits for a given Z_{HH} and Z_{DR}, and suggests that determining the contribution that a habit has to the reflectivity may be a more feasible approach.

6. Summary and Conclusions

This paper presented analyses of the microphysical properties of ice particles derived from data collected by cloud probes installed on the NSF/NCAR C-130 aircraft within the comma head of two winter cyclones in conjunction with ground-based radar data collected by the MAX 3.17 cm radar during RHI scans through the same plane as the aircraft's flight path. This sampling strategy allowed for the direct comparison of particle sizes, shapes, and habits with polarization variables Z_{HH} and Z_{DR} in the same region. Distributions of estimated particle reflectivity Z_p provided insight into the size characteristics for each crystal type and how they relate to Z_{HH}, while particle axis ratio α and sphericity β gave information about the shape for each habit and how they influence Z_{DR}. These derived in-situ properties were sorted into thirteen Z_{HH} and eight Z_{DR} bins encompassing -11 $< Z_{HH} <$ 15 dBZ and 0 $< Z_{DR} <$ 4 dB, which permitted computation of each habit's contribution to the total reflectivity, the reflectivity-weighted mean axis ratio $\bar{\alpha}$ and sphericity $\bar{\beta}$ from particles sampled within each binned interval.

The key findings of the paper are as follows:

1) No dominant crystal habits were observed for the majority of radar Z_{HH} and Z_{DR} measurements, with only 40% of the Z_{HH}-Z_{DR} bins having a habit contribute over 50% to the reflectivity in that bin. Of these bins, only 12% had a habit contribute over 75% to the reflectivity.

2) Differences in particle mass according to whether it was estimated from the particle's projected area or habit-dependent mass-diameter relations yielded up to an 11.73 dB difference in Z_p for habits such as bullet rosettes and graupel. This highlights the need to know particle density for accurate estimates of reflectivity. Mass estimates using the particle's projected area yielded derived reflectivities closer to Z_{HH} values than habit-dependent mass-diameter relations for the 14-15 February cyclone (19% lower RMSE), with the opposite result for the 21-22 February cyclone (5% lower RMSE using the mass

estimated from the projected area).

3) The coexistence of bullet rosettes and aggregates for $Z_{HH} > 7$ dBZ and $Z_{DR} > 2$ dB are consistent with the findings of previous studies (e.g., Hobbs et al. 1974). Their coexistence suggests that bullet rosettes are favored for aggregate formation.

4) Irregular particles made the largest contributions of any shape to the calculated reflectivity, with contributions ranging from 3 to 72% with a mean of 36%. However, only 55% of the Z_{HH}-Z_{DR} bins had irregular crystals contribute to over 40% of the reflectivity in that bin.

5) Greater contributions by bullet rosettes and aggregates for $Z_{HH} > 7$ dBZ and $Z_{DR} > 2$ dB along with α (β) values being higher (lower) than other habits yielded $\bar{\alpha}$ values as high as 1.3 and $\bar{\beta}$ values as low as 0.09. Contributions of hexagonal plates and graupel to the reflectivity exceeded 50% for 47% of the bins where $Z_{HH} < 1$ dBZ, causing $\bar{\alpha}$ values to be as low as 0.9 and $\bar{\beta}$ values as high as 0.25.

Given that no particular crystal habit contributes over 80% to the reflectivity for a given Z_{HH} and Z_{DR} value, assigning a single hydrometeor species to a particular radar pixel may not be the most appropriate technique. Furthermore, determining the probability of specific habits in radar volumes may be more suitable than the deterministic methods currently used.

Further studies utilizing sampling strategies that collect coincident radar and microphysical data in other cloud and meteorological environments may help to further understand the dependence of microphysical properties on polarization variables as well as to assess the validity of forward simulations of radar variables from microphysical data (e.g., Wolde et al. 2003; Kollias et al. 2011; Tyynelä et al. 2011; Zong et al. 2013).

Tables

Flight Legs with Coincident Data

14-15 February			21-22 February		
# Obs. in Cloud	Alt. (km)	Temp. (°C)	# Obs. in Cloud	Alt. (km)	Temp. (°C)
21	6.80	-44	17	7.59	-39
29	5.88	-36	15	6.84	-31
41	5.05	-29	34	6.19	-24
47	4.14	-22	31	5.74	-20
45	3.26	-16	45	5.16	-17
14	2.65	-14			
5	5.90	-48			
13	7.31	-49			
2	6.43	-41			
19	5.49	-35			
45	4.43	-29			
62	3.47	-24			

Table 1: Summary of constant-altitude flight legs coincident with MAX radar data acquired during the 14-15 and 21-22 February events. For each constant altitude leg through the system, the number of coincident observations in the cloud, mean altitude (km), and mean temperature (°C) are listed.

	14-15 February				21-22 February			
Habit	$Z_{p,JA14}$	$Z_{p,BL06}$	α	β	$Z_{p,JA14}$	$Z_{p,BL06}$	α	β
Irregular	0.160	0.096	0.093	0.102	**0.340**	**0.275**	0.085	0.194
Bullet Rosette	0.162	0.120	0.073	0.185	**0.241**	**0.211**	0.060	0.141
Aggregate	0.039	0.015	0.004	0.133	0.119	0.180	0.013	0.032
Hexagonal	0.108	0.134	0.081	0.005	0.159	**0.202**	0.109	0.005
Graupel	0.014	0.011	0.004	0.017	0.016	0.080	0.015	0.137
Linear	0.136	0.082	0.086	0.125	**0.234**	0.172	0.118	0.171
Oriented	0.142	0.130	0.080	0.147	**0.241**	**0.224**	0.164	0.083
Spherical	0.035	0.069	0.011	0.040	0.117	0.114	0.049	0.002
ALL	0.048	0.074	0.095	0.114	0.096	**0.211**	0.142	**0.244**

Table 2: Cohen's d effect size for distributions from particles sampled during coincident timeframes versus the entire flight for the 14-15 and 21-22 February events. Values around 0.2 or less indicate a statistically small difference between two distributions (Cohen 1988), with values above this suggested threshold in bold.

Habit	$Z_{p,JA14}$	$Z_{p,BL06}$	α	β
Irregular	**0.240**	0.084	0.074	0.191
Bullet Rosette	**0.246**	0.194	0.005	0.095
Aggregate	**0.977**	**0.556**	0.009	**0.715**
Hexagonal	0.157	0.130	0.142	**0.230**
Graupel	**0.223**	**0.228**	0.072	**0.329**
Linear	0.082	0.066	0.115	0.121
Oriented	0.016	0.014	0.163	**0.229**
Spherical	**0.293**	**0.664**	**0.397**	**0.241**
ALL	0.032	0.085	0.091	0.022

Table 3: Same as in Table 2, but for coincident distributions between both events.

Figures

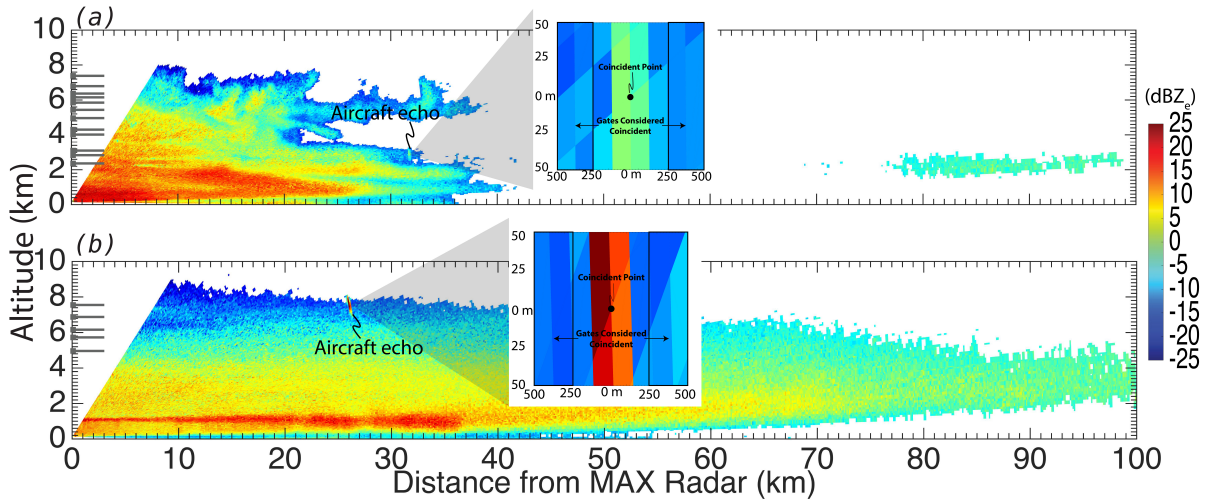

Figure 1: RHI scan of equivalent radar reflectivity (dBZ_e) at (a) 0657 UTC 15 February and (b) 0104 UTC 22 February with an aircraft echo indicating the C-130 aircraft's position at the time the scan was conducted. The inset shows a 1 km x 100 m region surrounding the aircraft's position with radar gates within the outlined boxes being considered coincident. Grey bars on the left axis denote altitudes of all aircraft flight legs during each event.

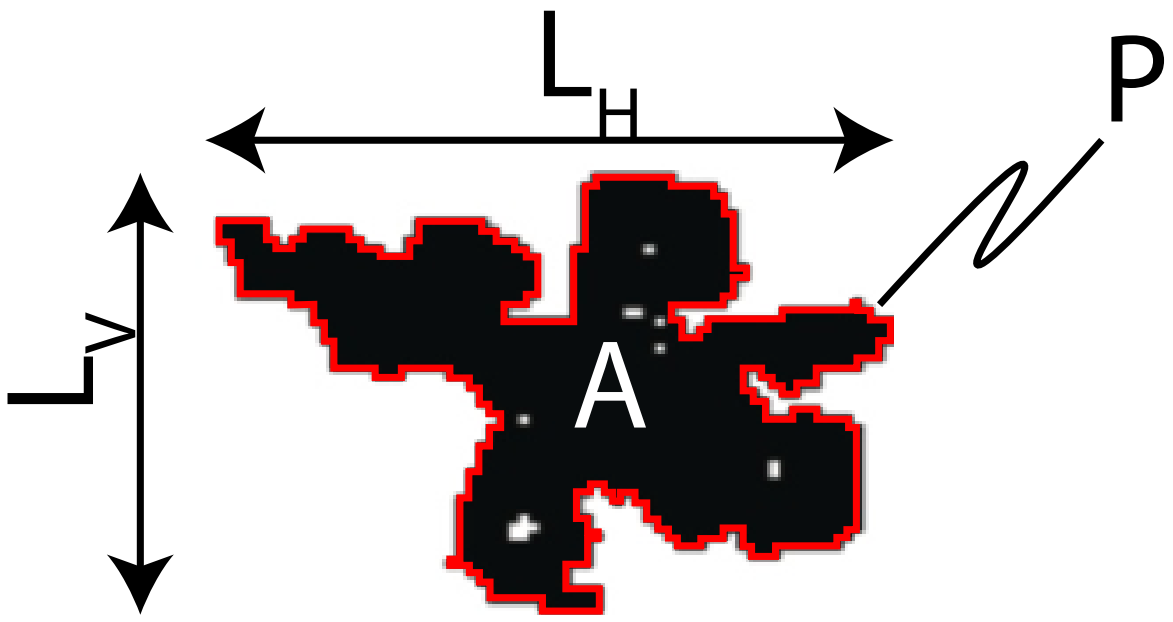

Figure 2: 2D-C particle image, with L_H denoting the particle length in the horizontal dimension, L_V the particle length in the vertical dimension, A the cross-sectional area, and P the perimeter.

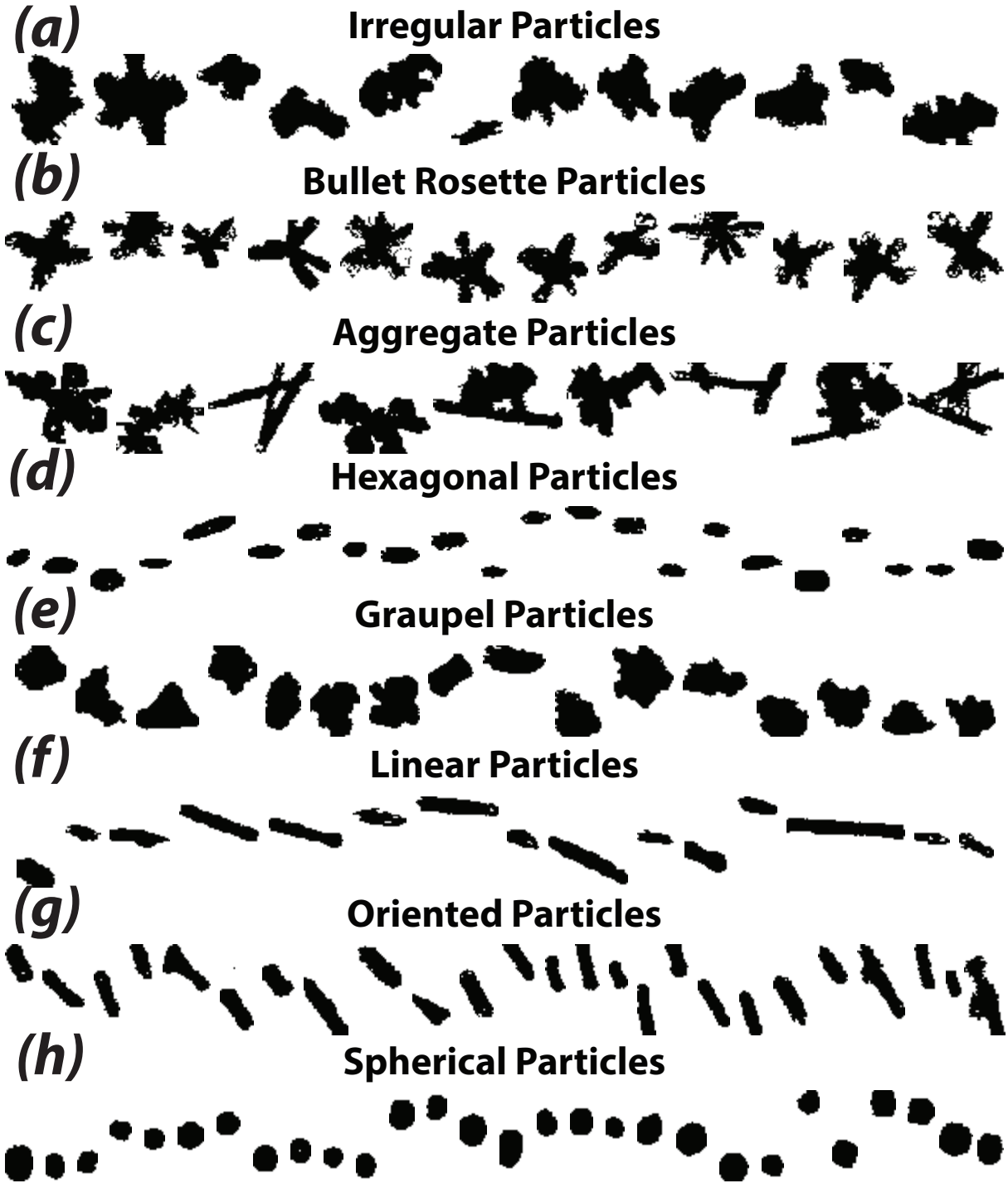

Figure 3: Representative particle images for (a) irregular, (b) bullet rosette, (c) aggregate, (d) hexagonal, (e) graupel, (f) linear, (g) oriented, and (f) spherical habits from the 2D-C probe.

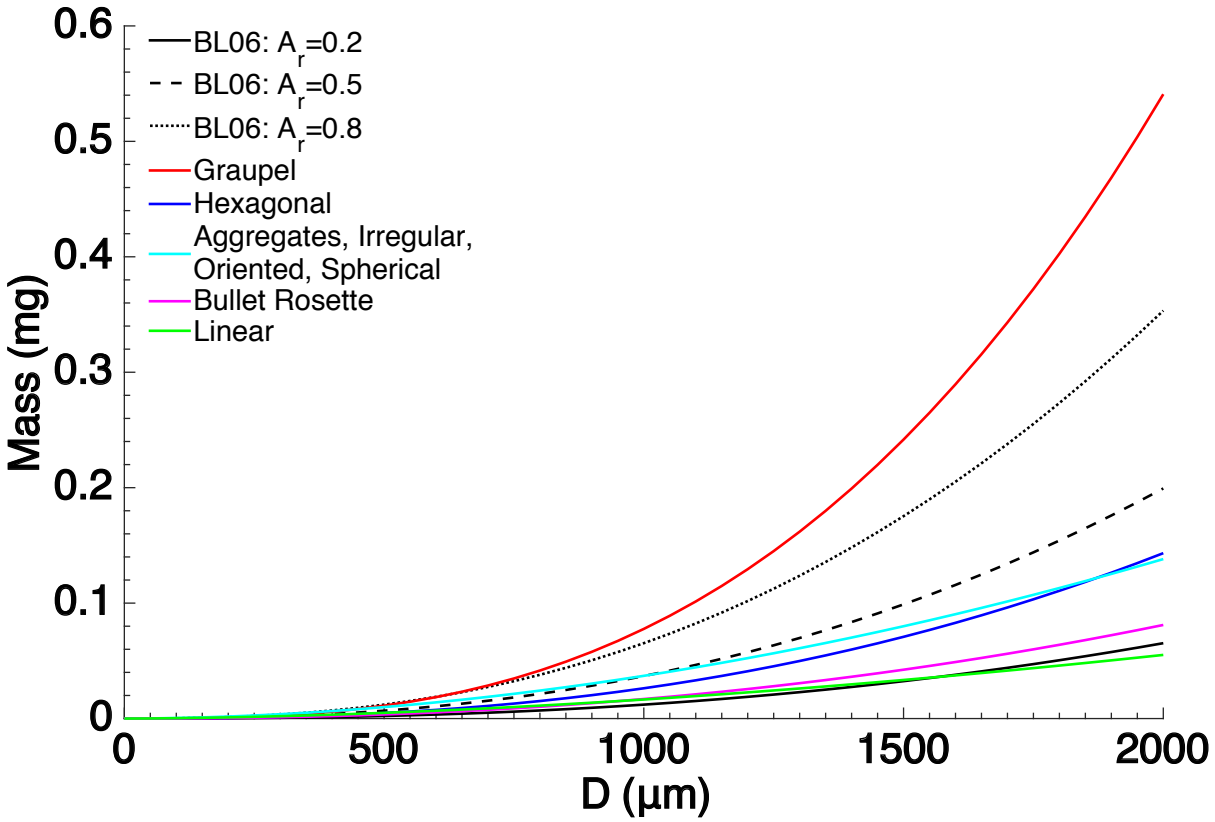

Figure 4: Mass of an individual particle as a function of D using two approaches in estimating m. Black curves represent m at varying A_r, while colored curves denote m-D relationships specific to each habit following McFarquhar et al. (2002).

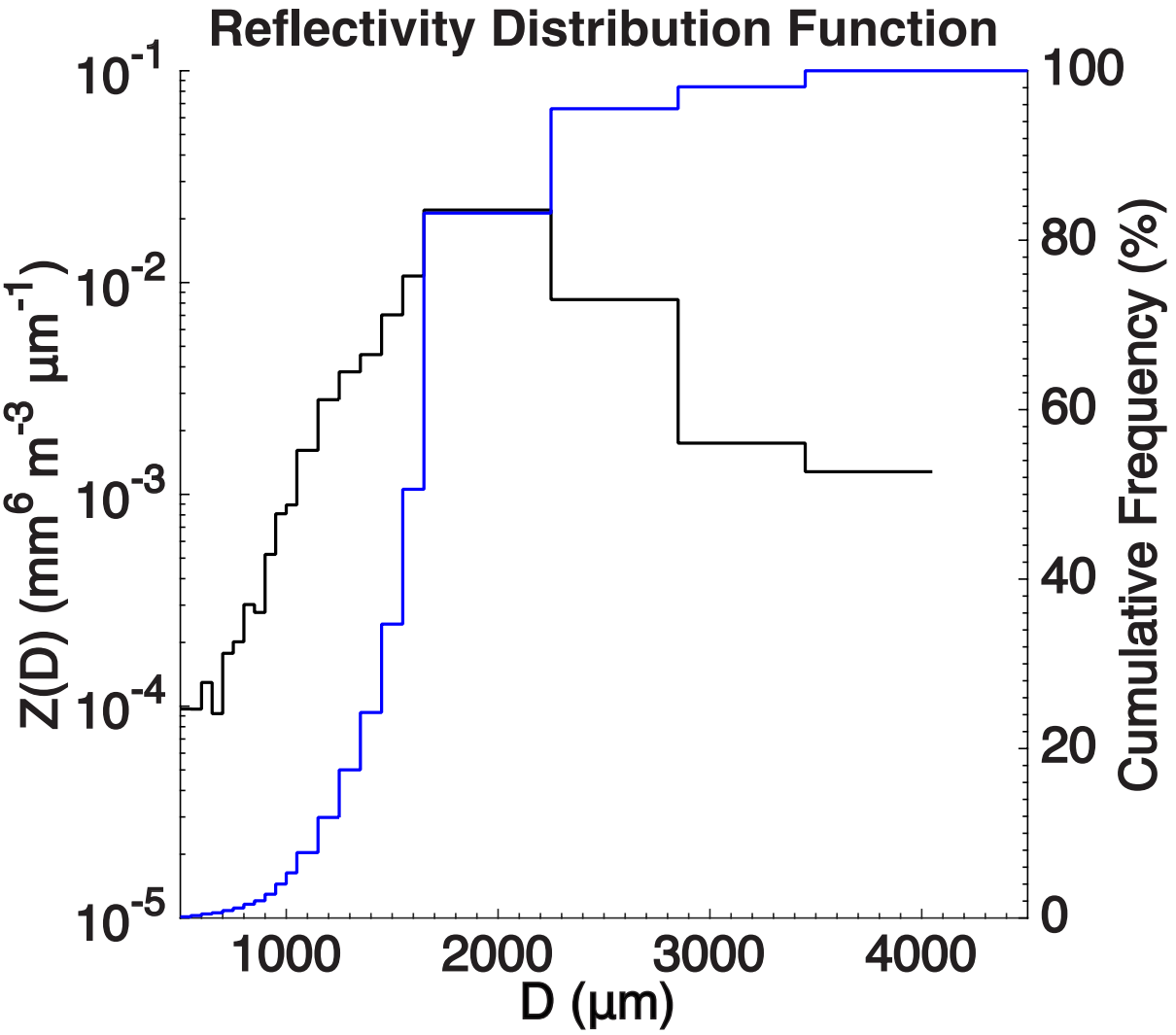

Figure 5: Reflectivity distribution function (black) and cumulative frequency (blue) during a 10-second interval at 0701 UTC on 15 February when the C-130 flew through a region of high Z_{HH} from a joint distribution spanning cloud and precipitation particle sizes using the mass relationship from Baker and Lawson (2006).

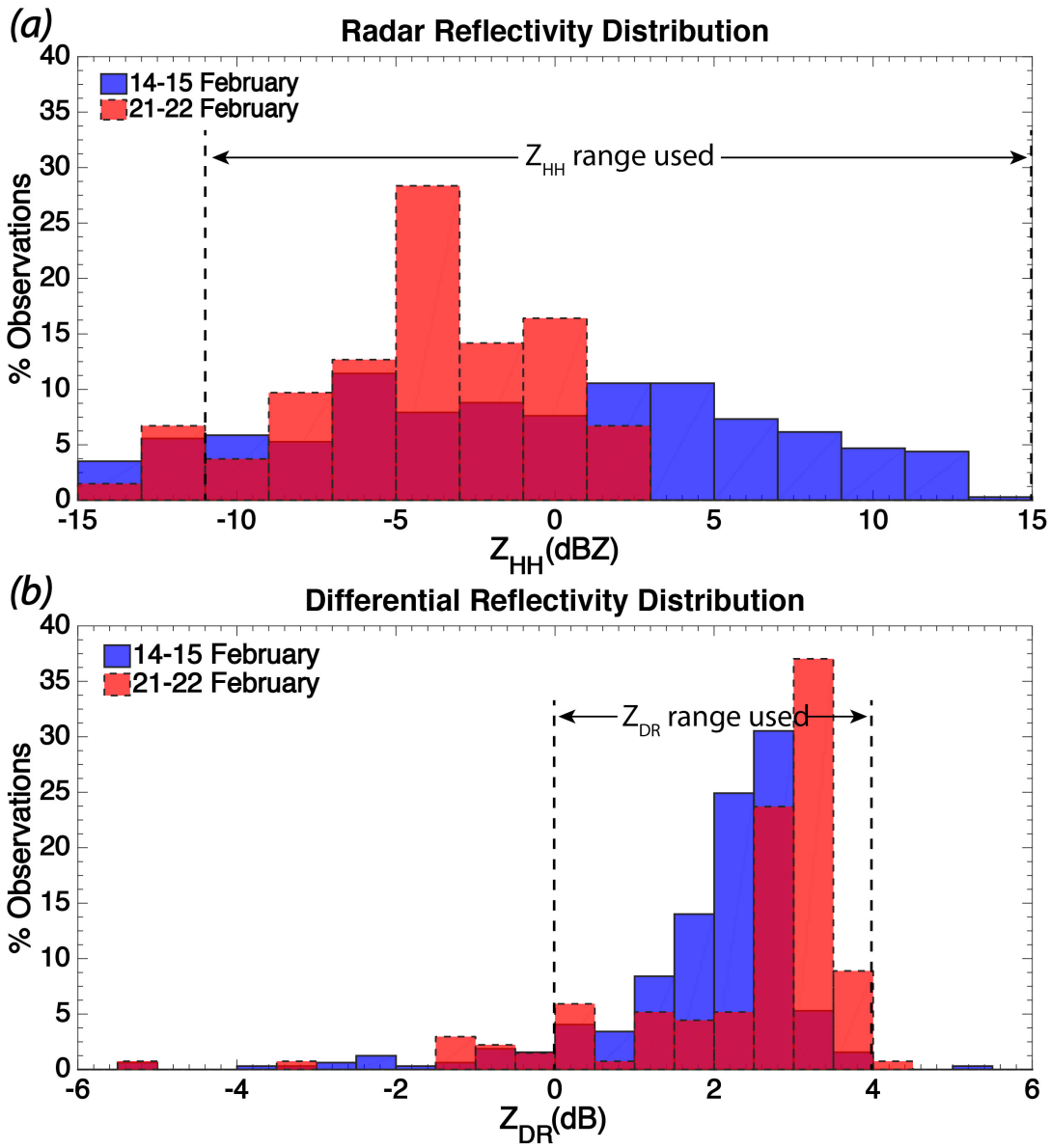

Figure 6: Distribution of (a) Z_{HH} and (b) Z_{DR} measurements for the 14-15 and 21-22 February events when the C-130 aircraft was coincident with the MAX radar. The range of Z_{HH} and Z_{DR} values chosen for the Z_{HH}-Z_{DR} domain are indicated.

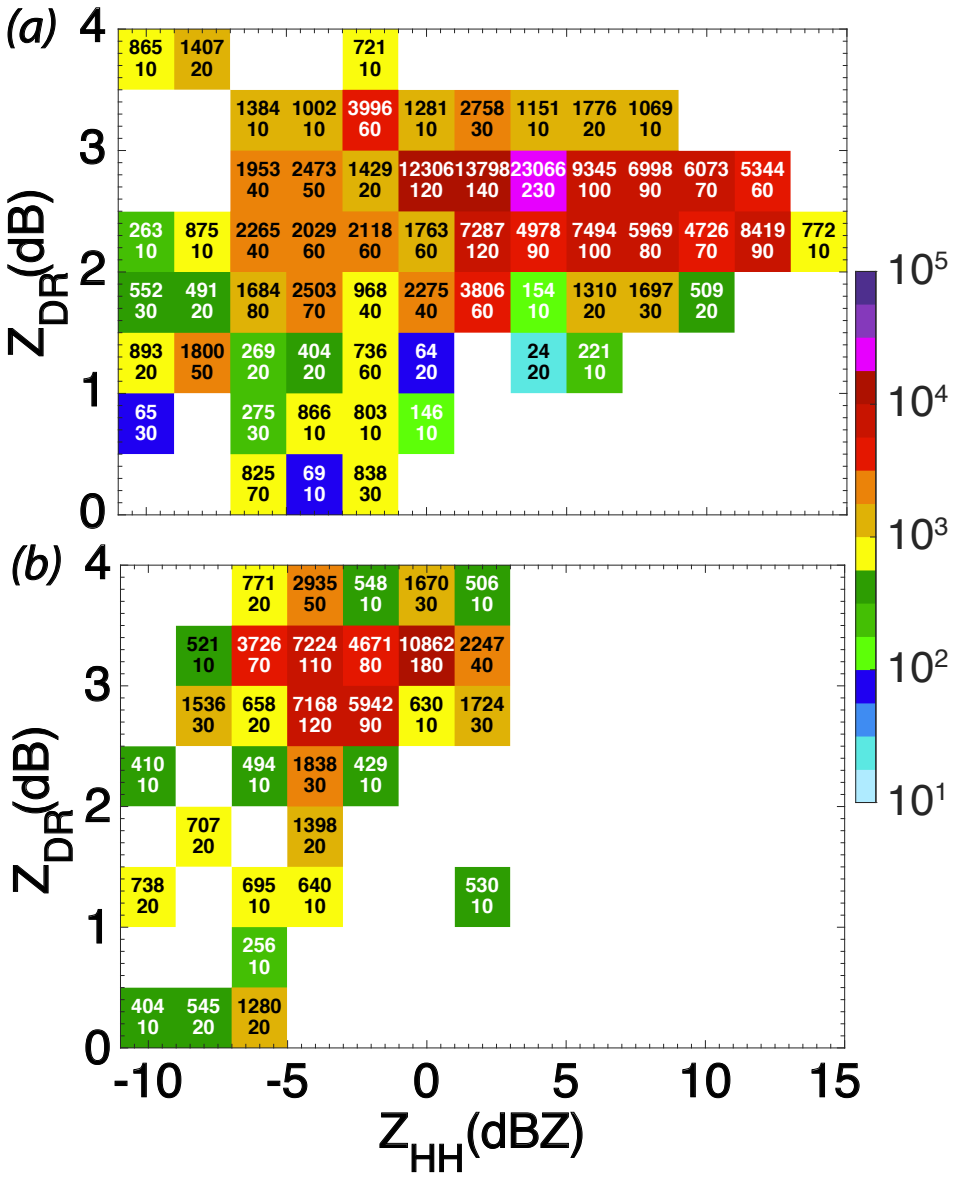

Figure 7: Number of accepted particles sampled by the 2D-C OAP (top, colored) and aircraft sampling duration (in seconds, bottom) during times when the aircraft was coincident with the MAX radar and within a particular Z_{HH}-Z_{DR} binned interval for (a) 14-15 and (b) 21-22 February 2010.

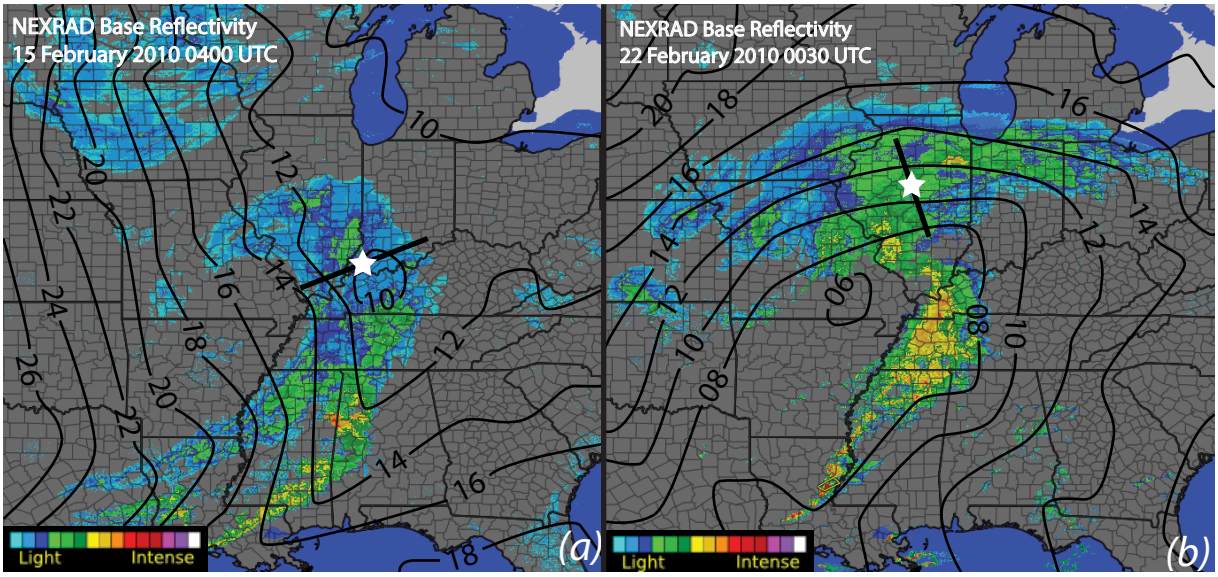

Figure 8: WSR-88D radar composites from (a) 0400 UTC 15 February 2010 and (b) 0030 UTC 22 February 2010. Overlaid on the image is the location of the MAX radar (white star), C-130 flight track and azimuthal angle of RHI scans (black line), and the sea level pressure field from Rapid Update Cycle model initialization at (a) 0400 and (b) 0000 UTC (black contours, hPa-1000).

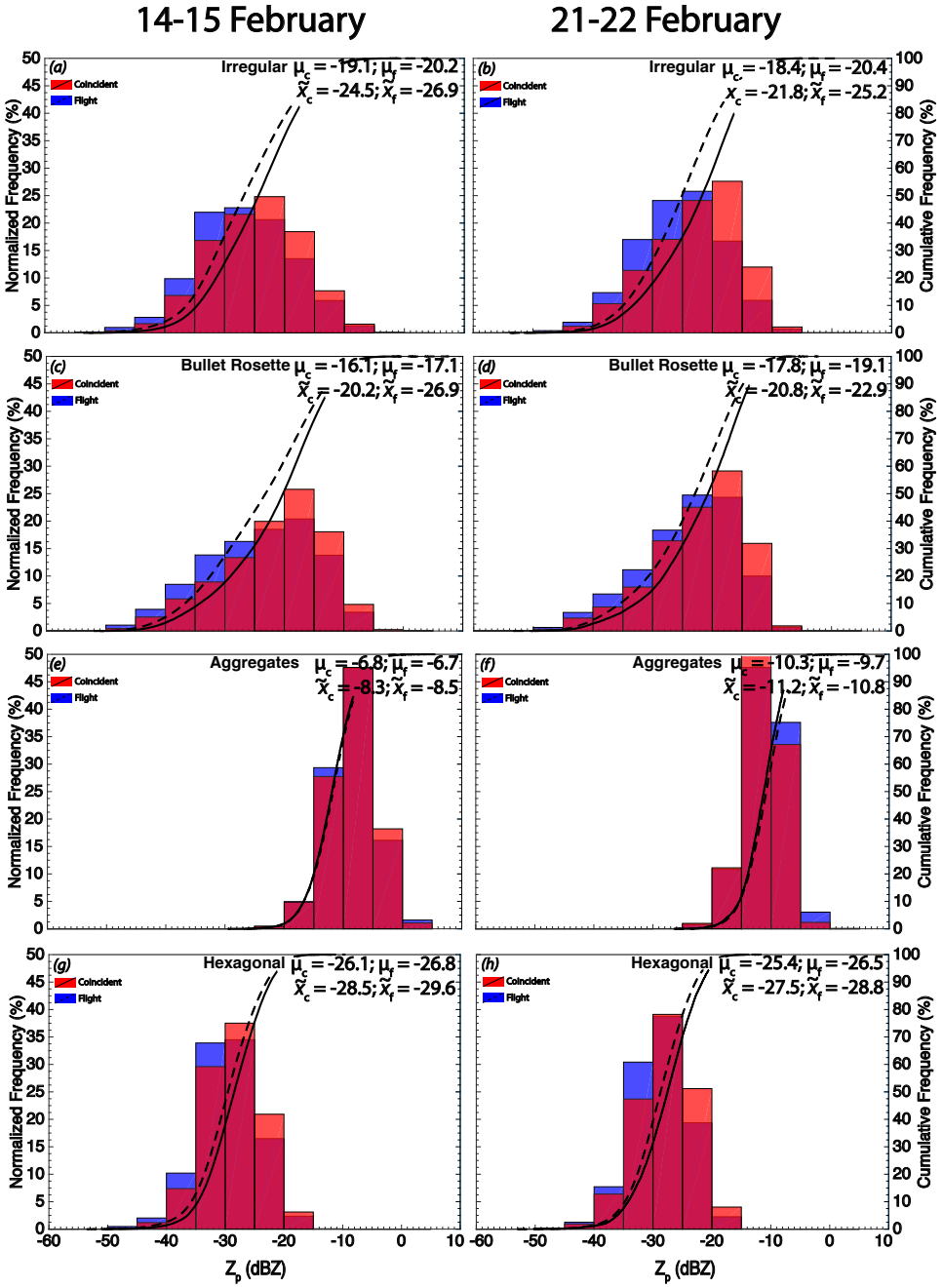

Figure 9: Z_p distribution (in dBZ) for the same eight habits as in Fig. 3 during coincident time frames and the entire sampling period for both cyclones using the mass relationship from Baker and Lawson (2006). Black curves denote the cumulative frequency of particles having a Z_p up to a particular value. Distribution mean and median for both datasets are shown.

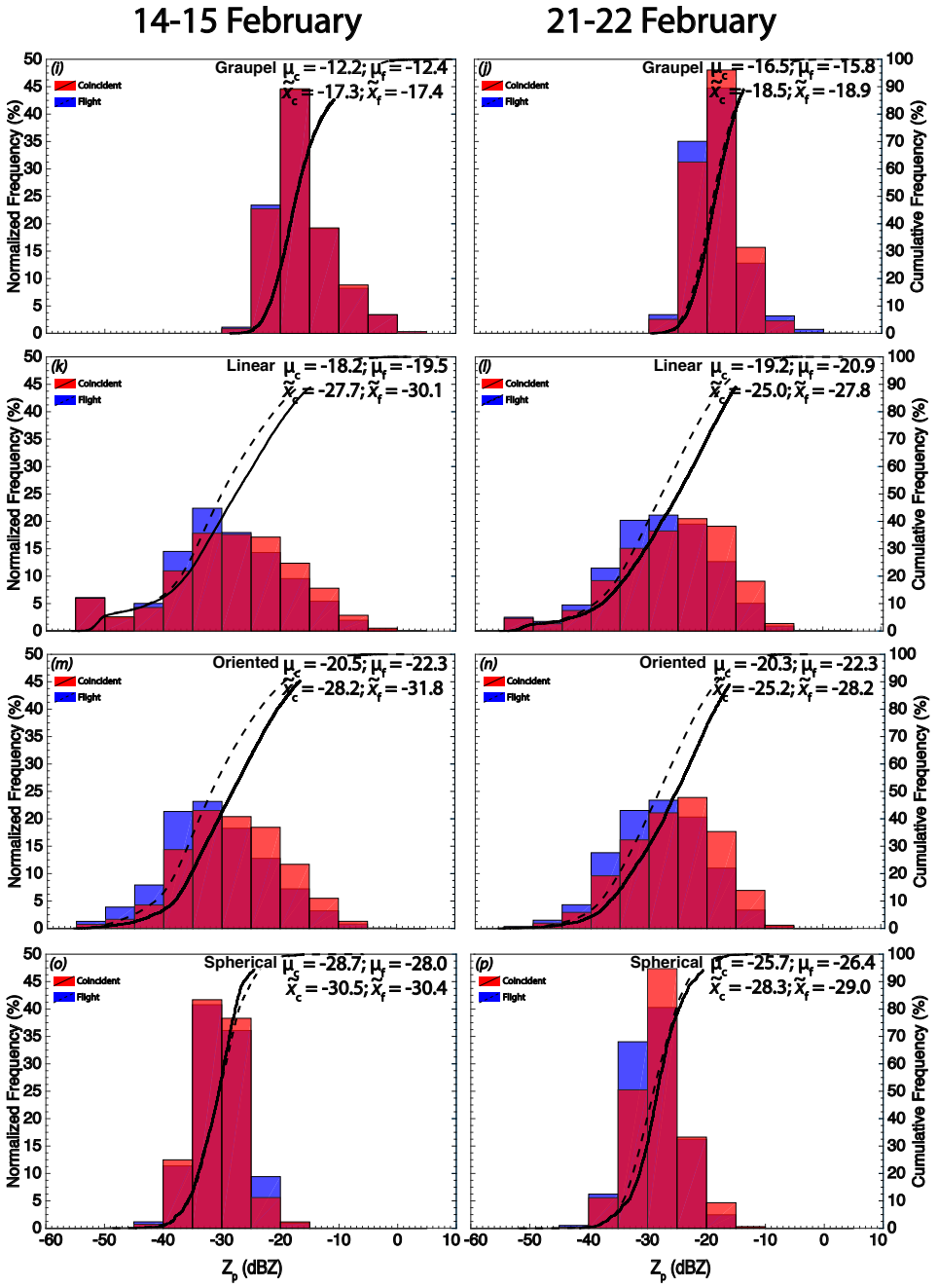

Figure 9: *(Continued.)*

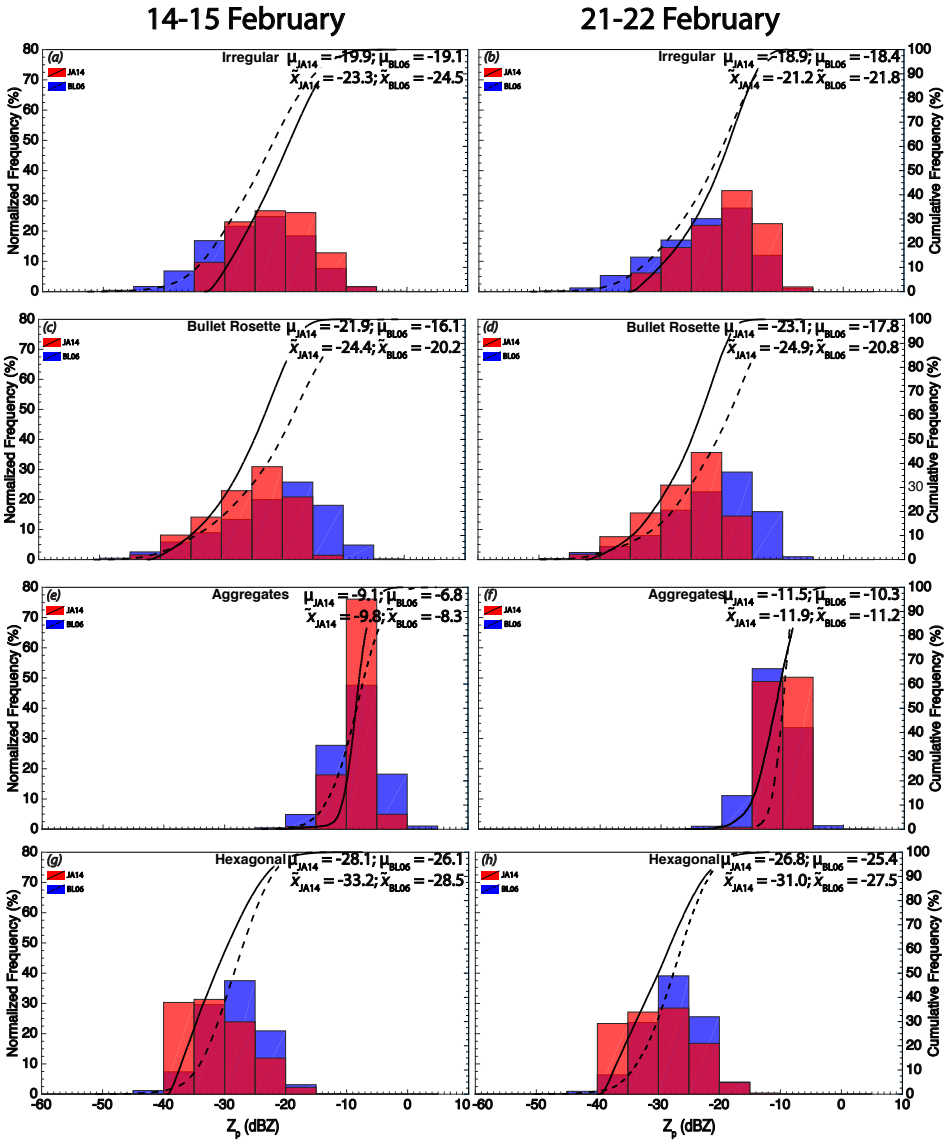

Figure 10: Same as in Fig. 9, but comparing Z_p using mass estimation methods from Baker and Lawson (2006) and McFarquhar et al. (2002) for particles sampled during coincident time frames.

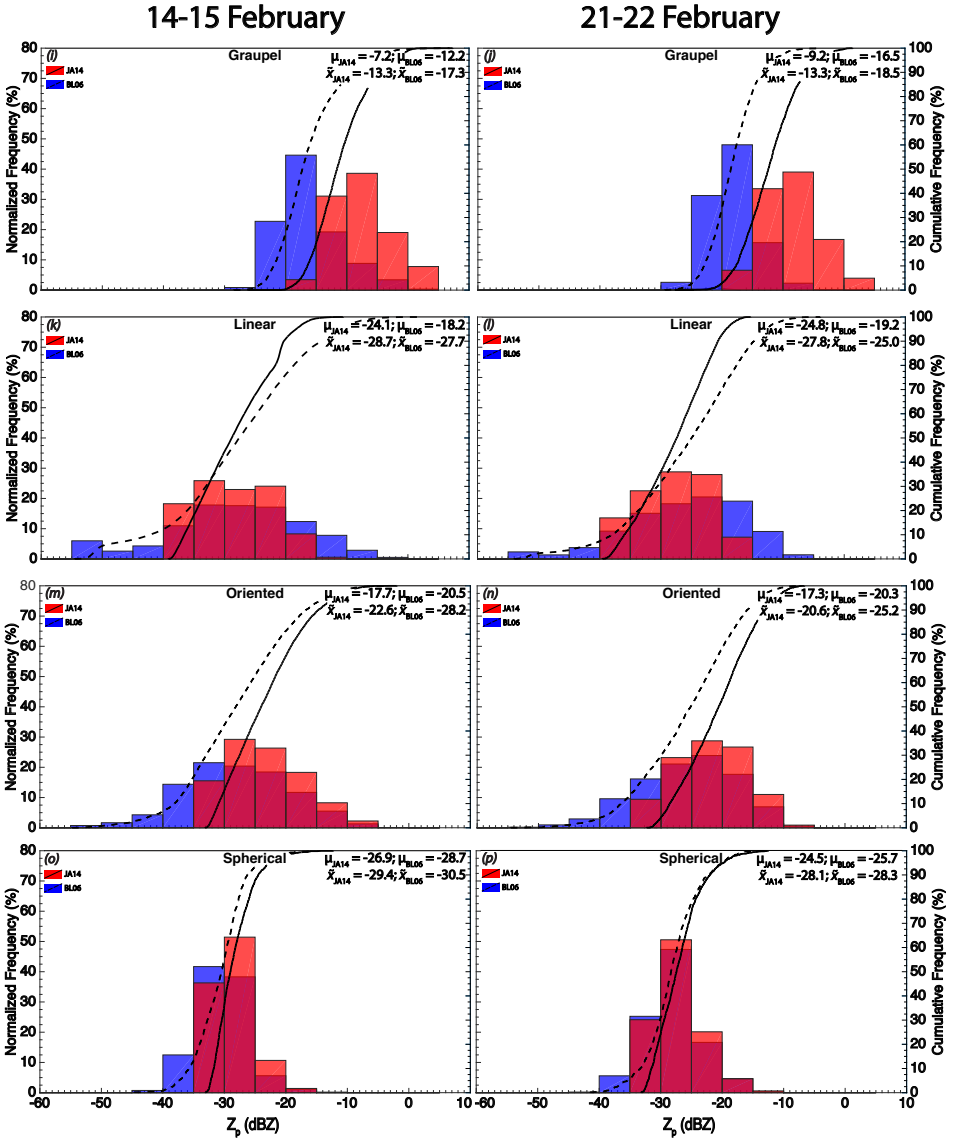

Figure 10: *(Continued.)*

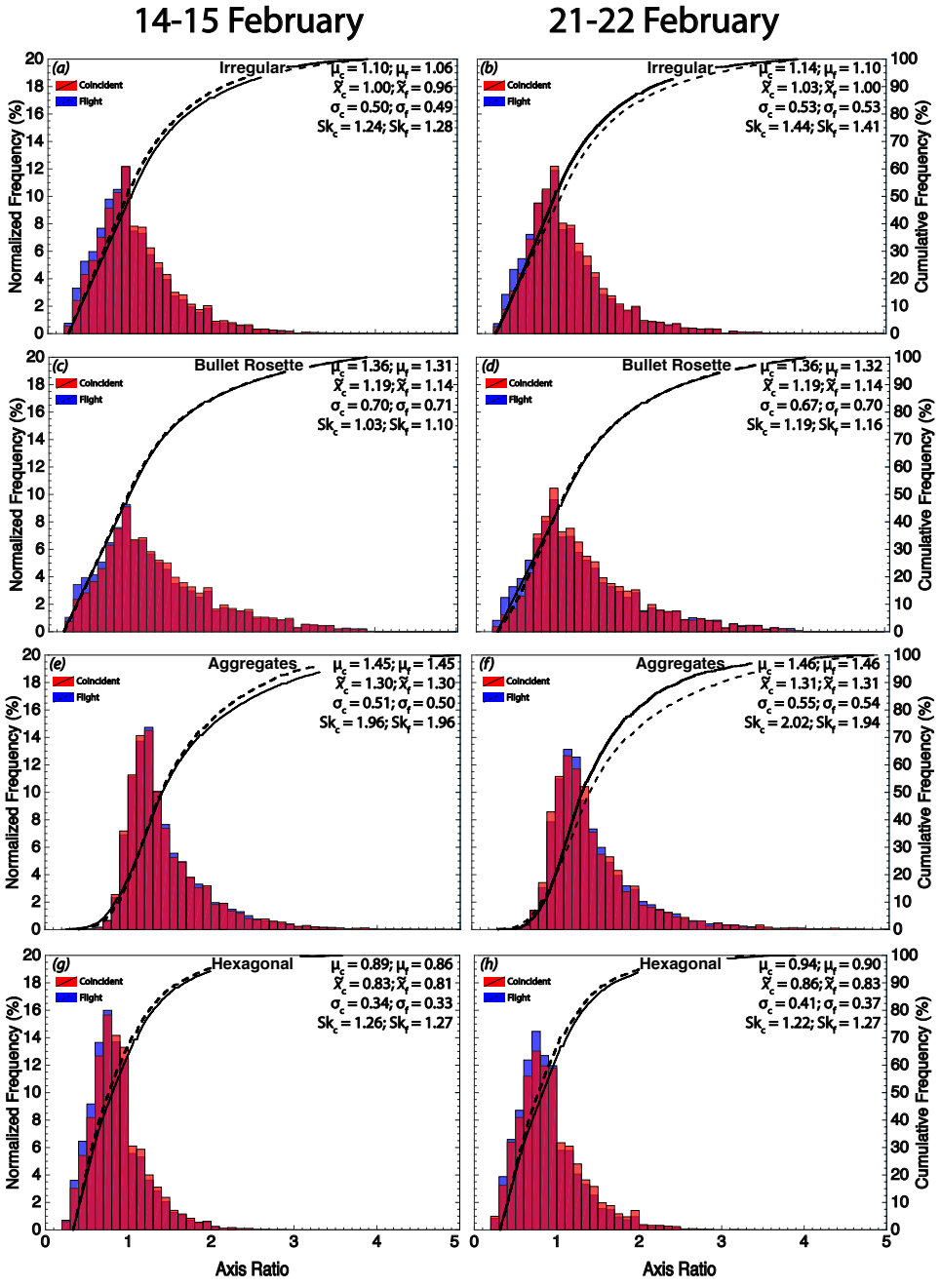

Figure 11: Same as in Fig. 9, but for α. Distribution standard deviation and skewness are also shown.

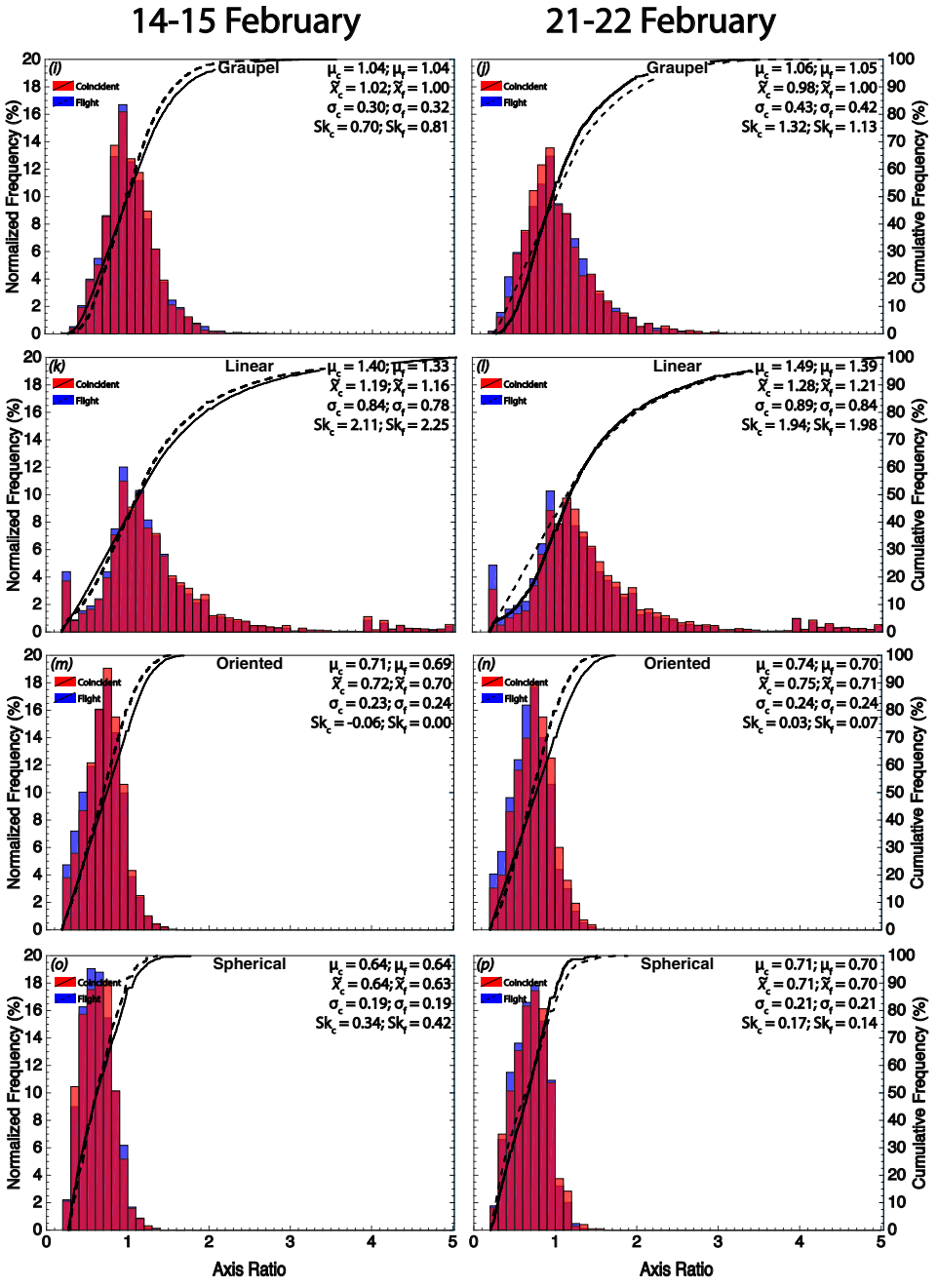

Figure 11: *(Continued.)*

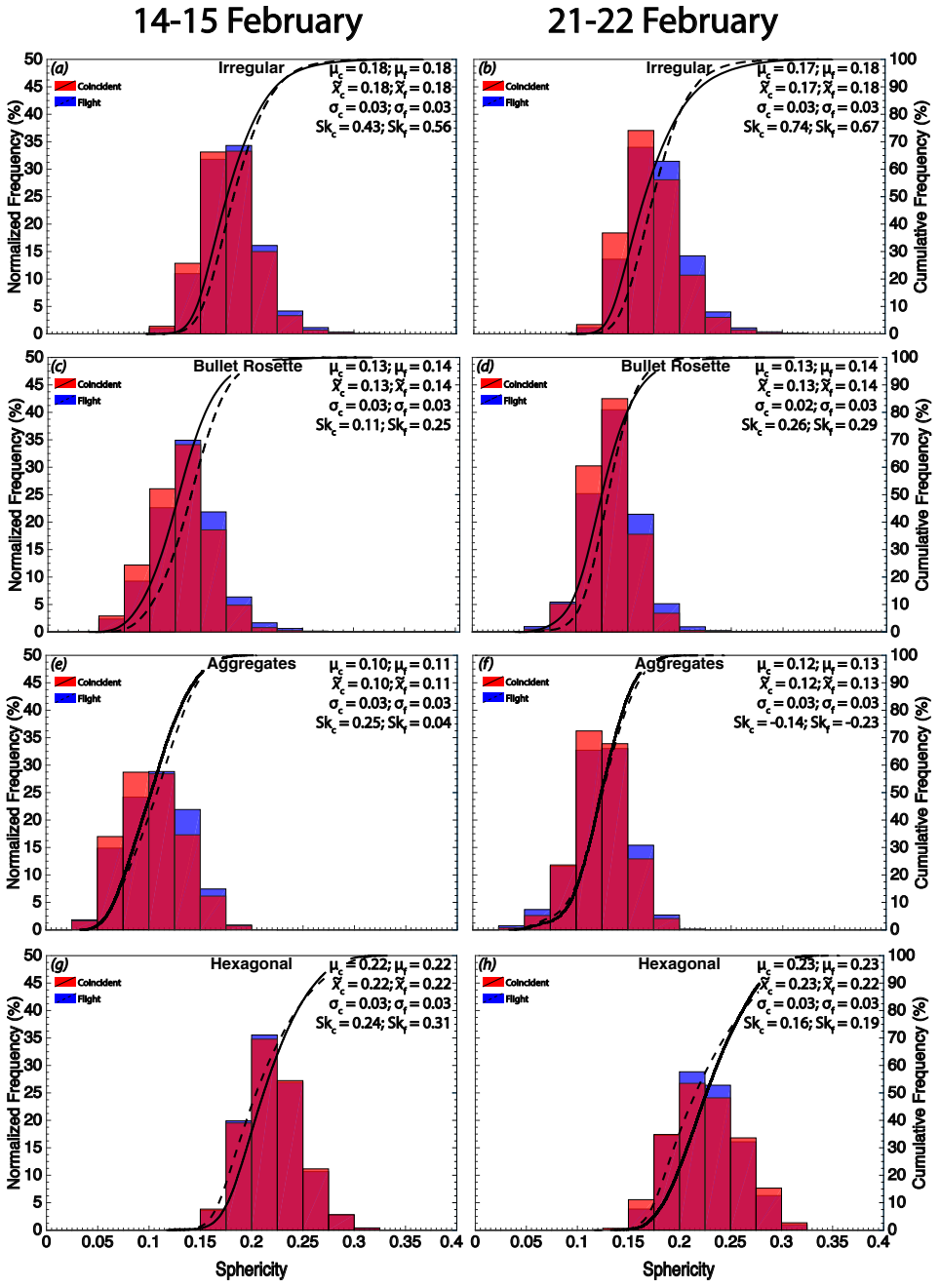

Figure 12: Same as in Fig. 11, but for β.

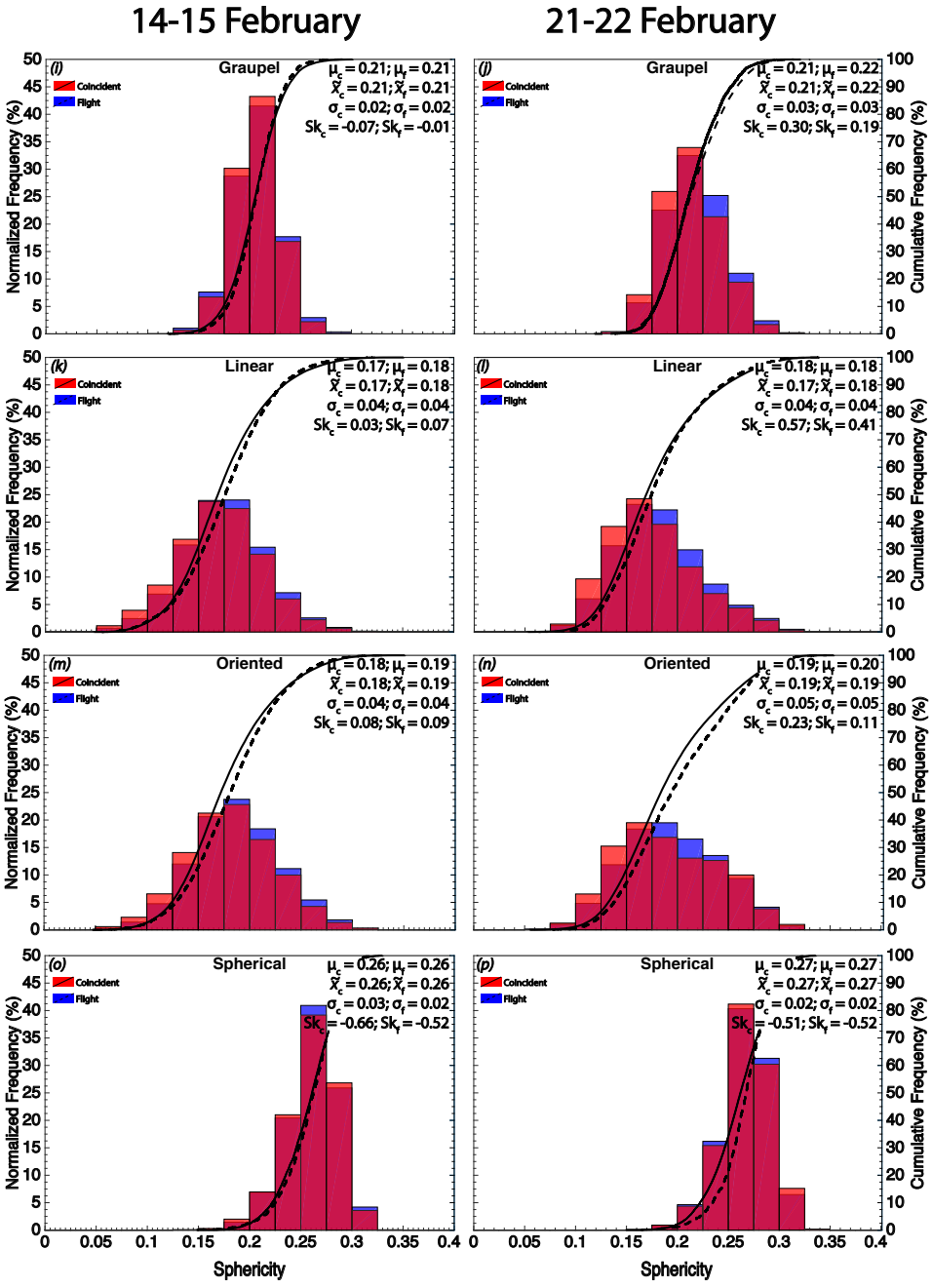

Figure 12: *(Continued.)*

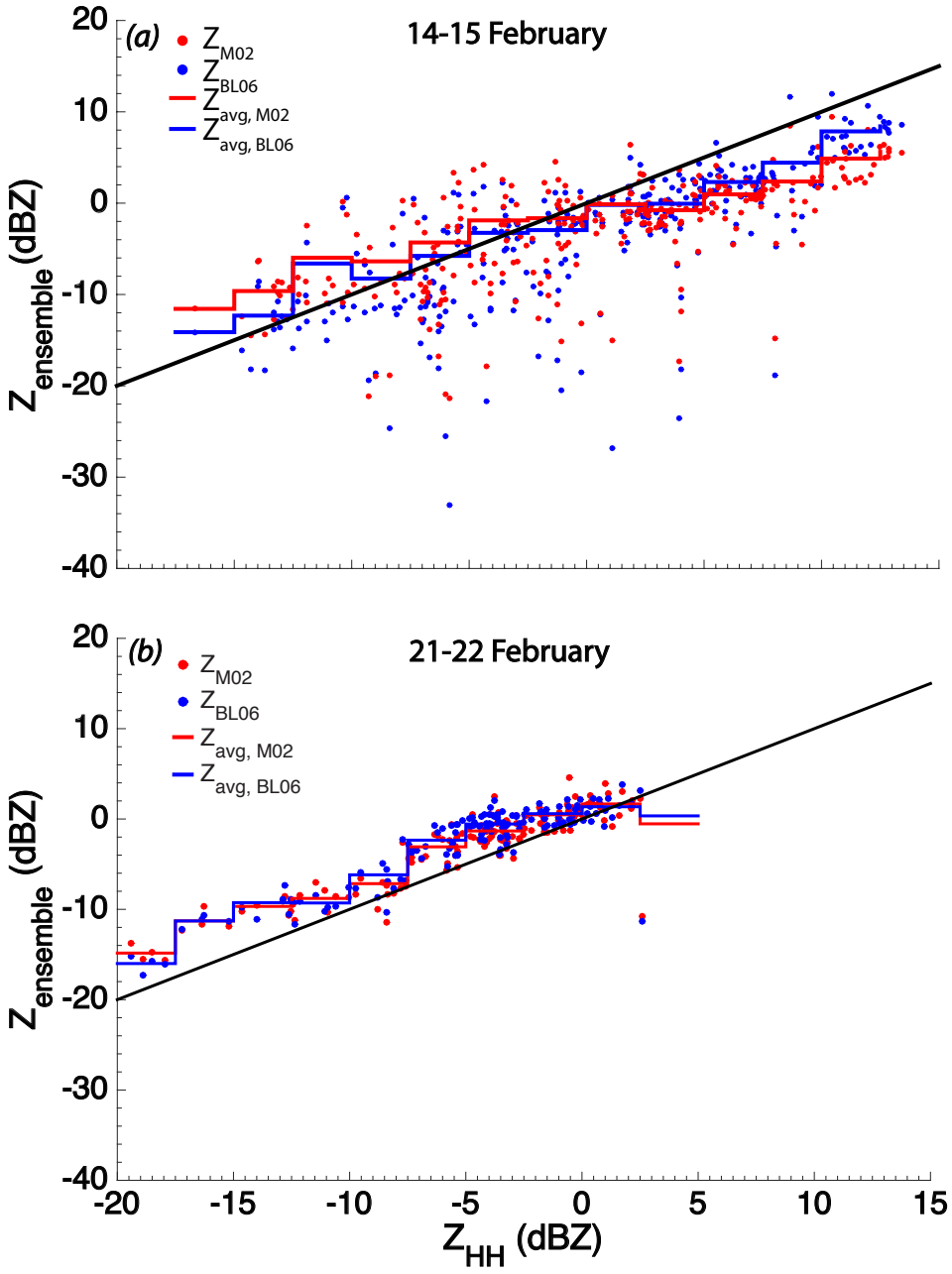

Figure 13: Reflectivity calculated from particles surrounding a coincident point ($Z_{ensemble}$) on (a) 14-15 and (b) 21-22 February using mass estimates based on habit-dependent m-D relations (M02) and the particle's projected area (BL06) compared to Z_{HH} measured from the MAX radar at the same location. Colored lines represent the mean $Z_{ensemble}$ value at coincident points corresponding to a Z_{HH} value within a 2.5 dB interval. The black line is the 1:1 line.

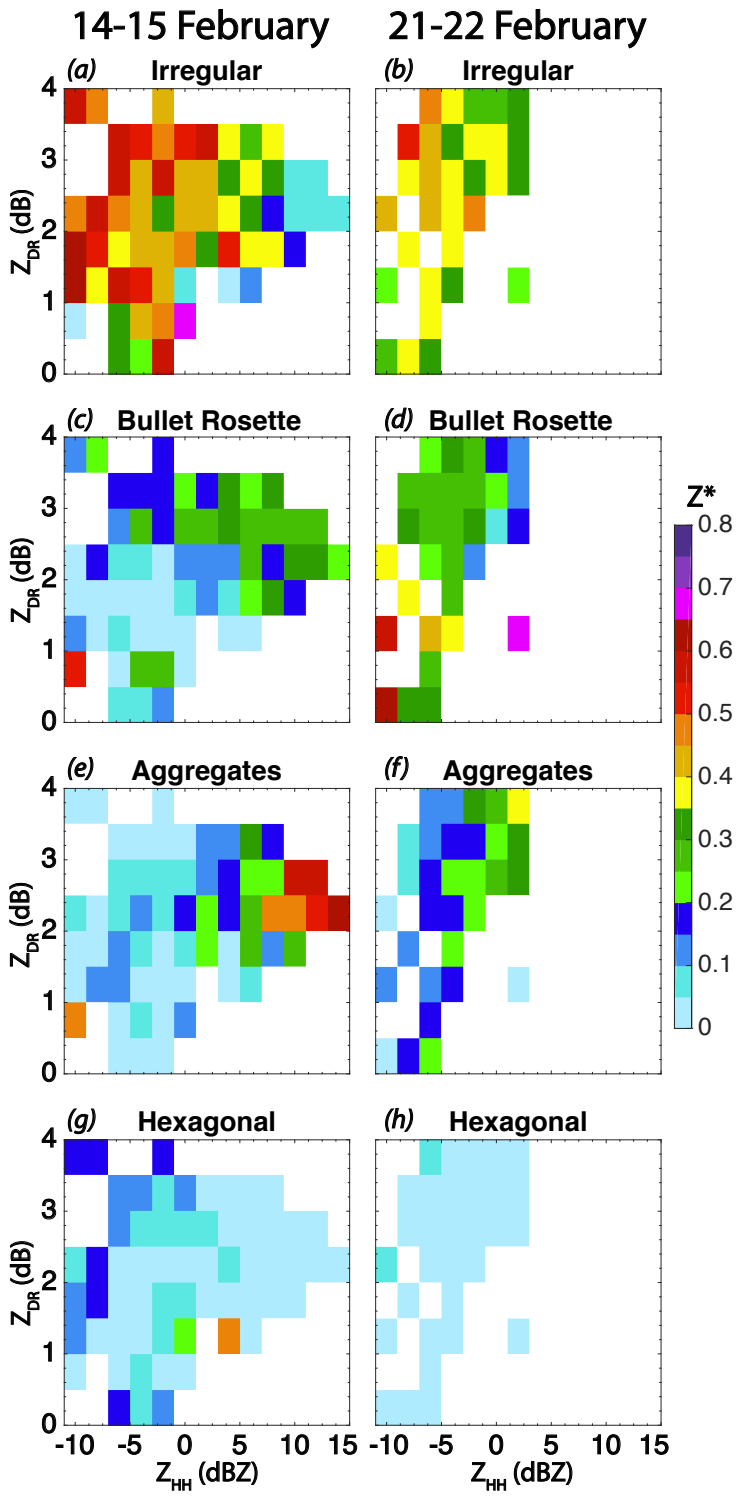

Figure 14: Contribution of a habit's calculated reflectivity using the mass-area relationship from BL06 to the total reflectivity for all particles coincident with radar measurements at specific Z_{HH} and Z_{DR} binned intervals.

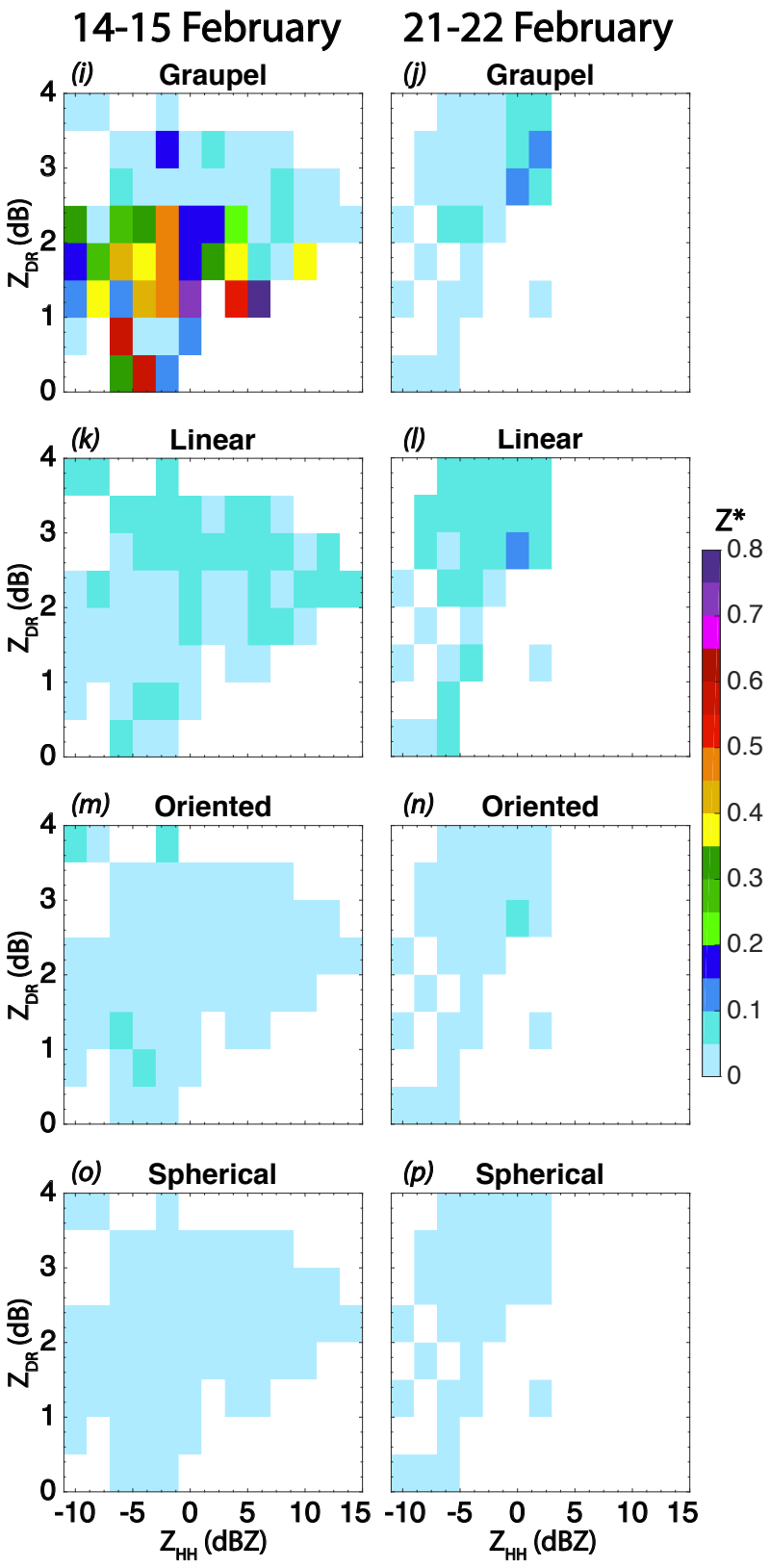

Figure 14: *(Continued.)*

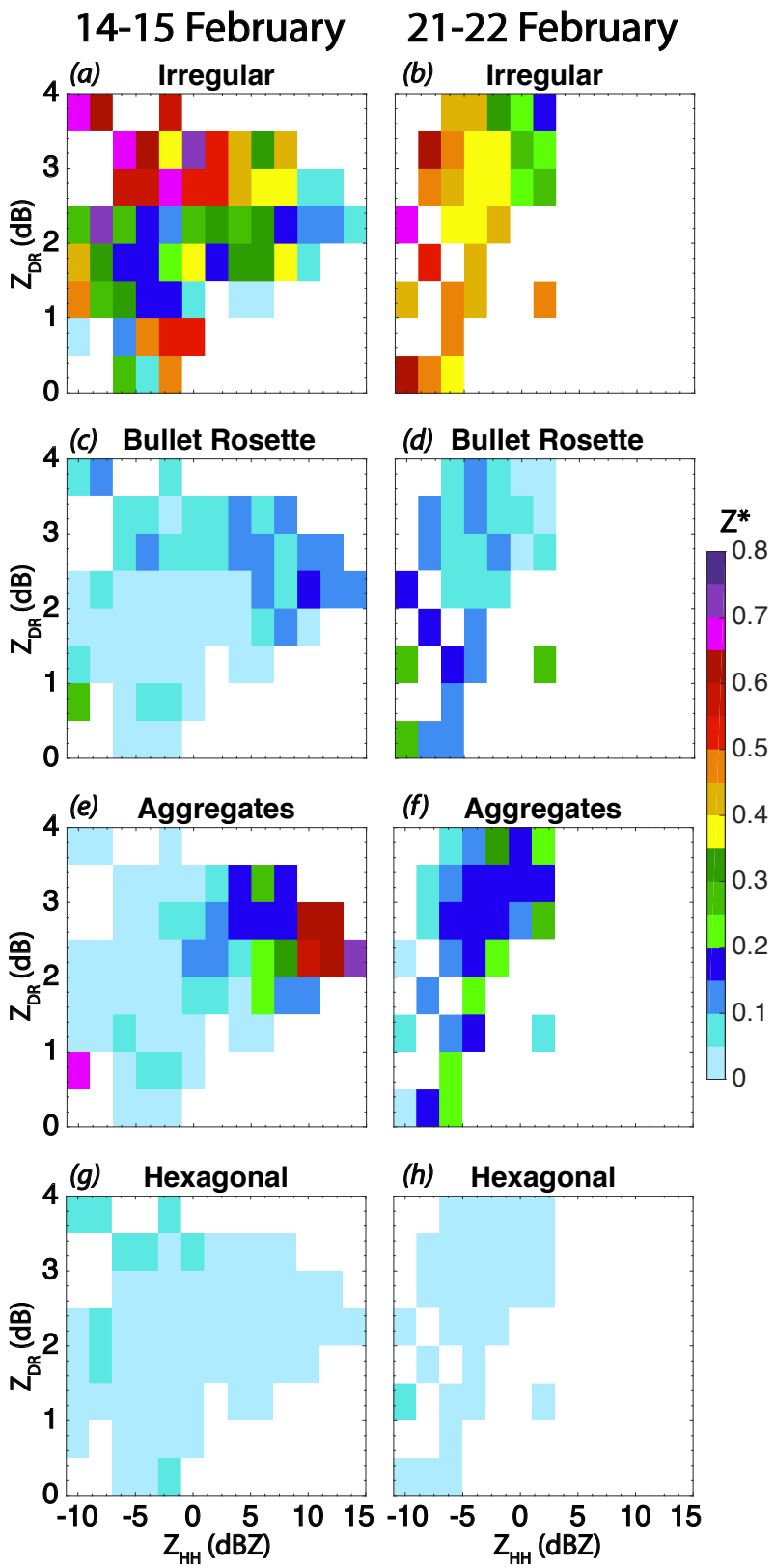

Figure 15: Same as in Fig. 14, but using habit-specific m-D relationships outlined in M02.

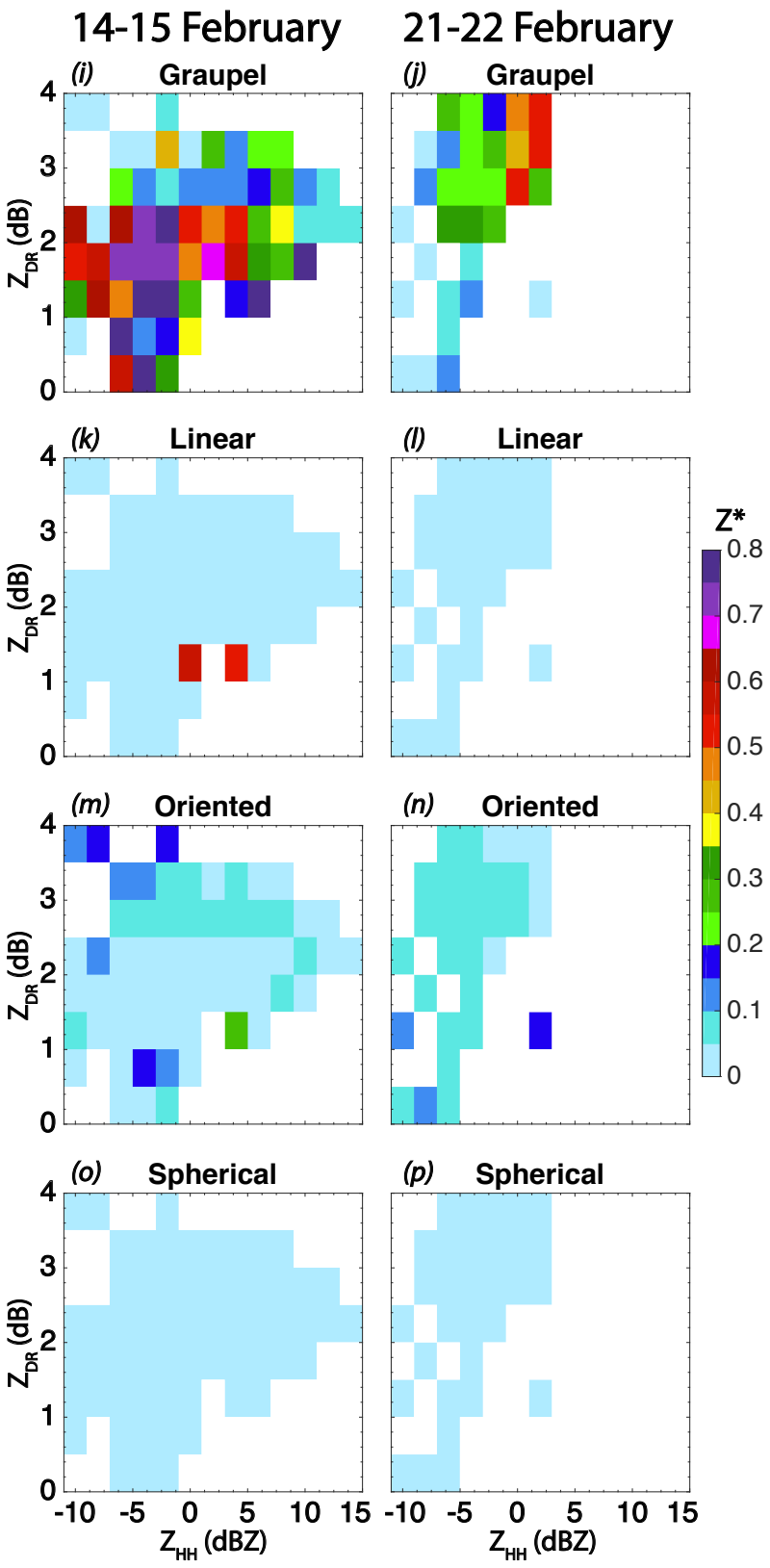

Figure 15: *(Continued.)*

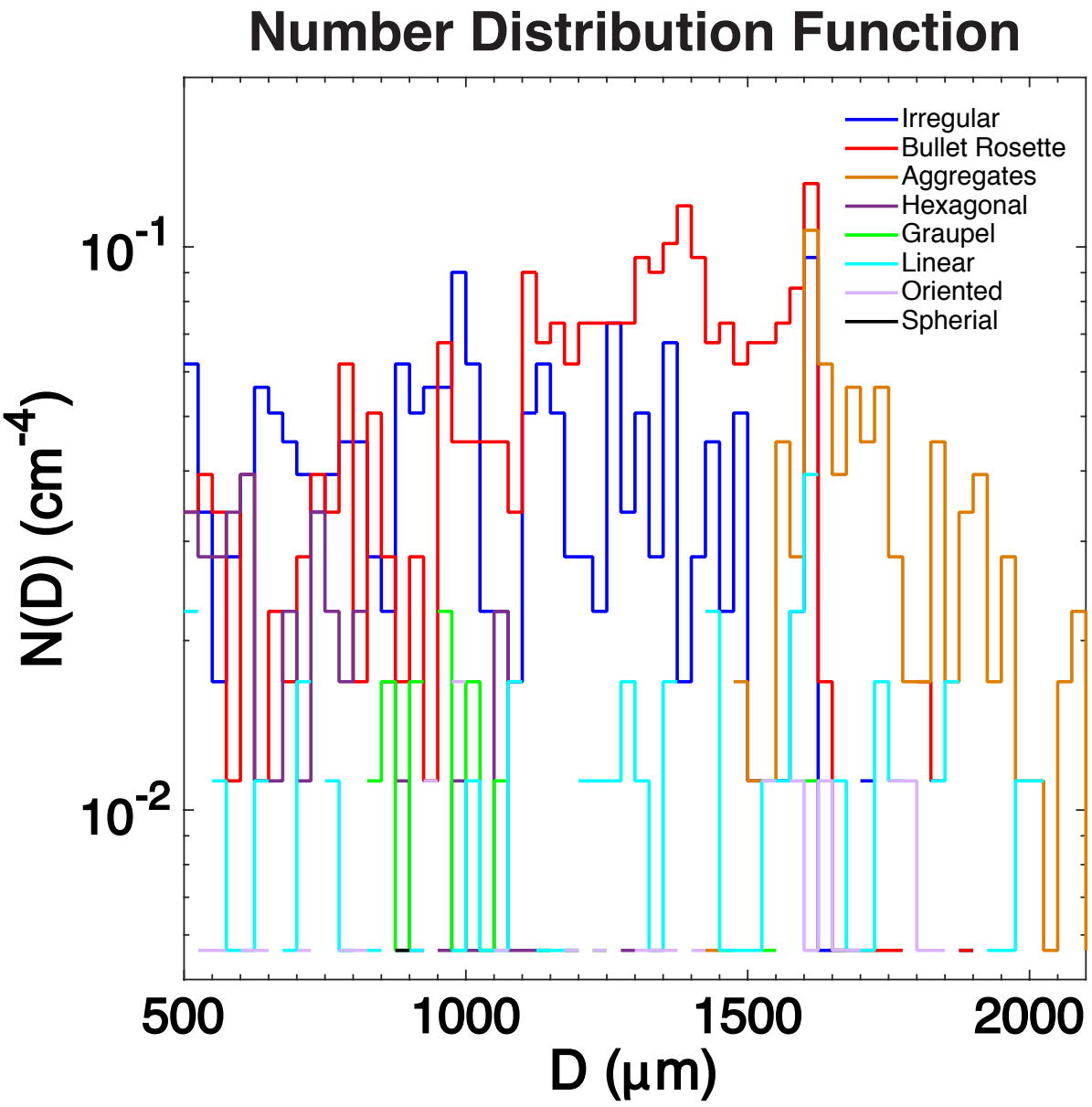

Figure 16: N(D) for each habit during the same 10-second interval as in Fig. 5 spanning cloud particle sizes 500 > D > 2100 μm.

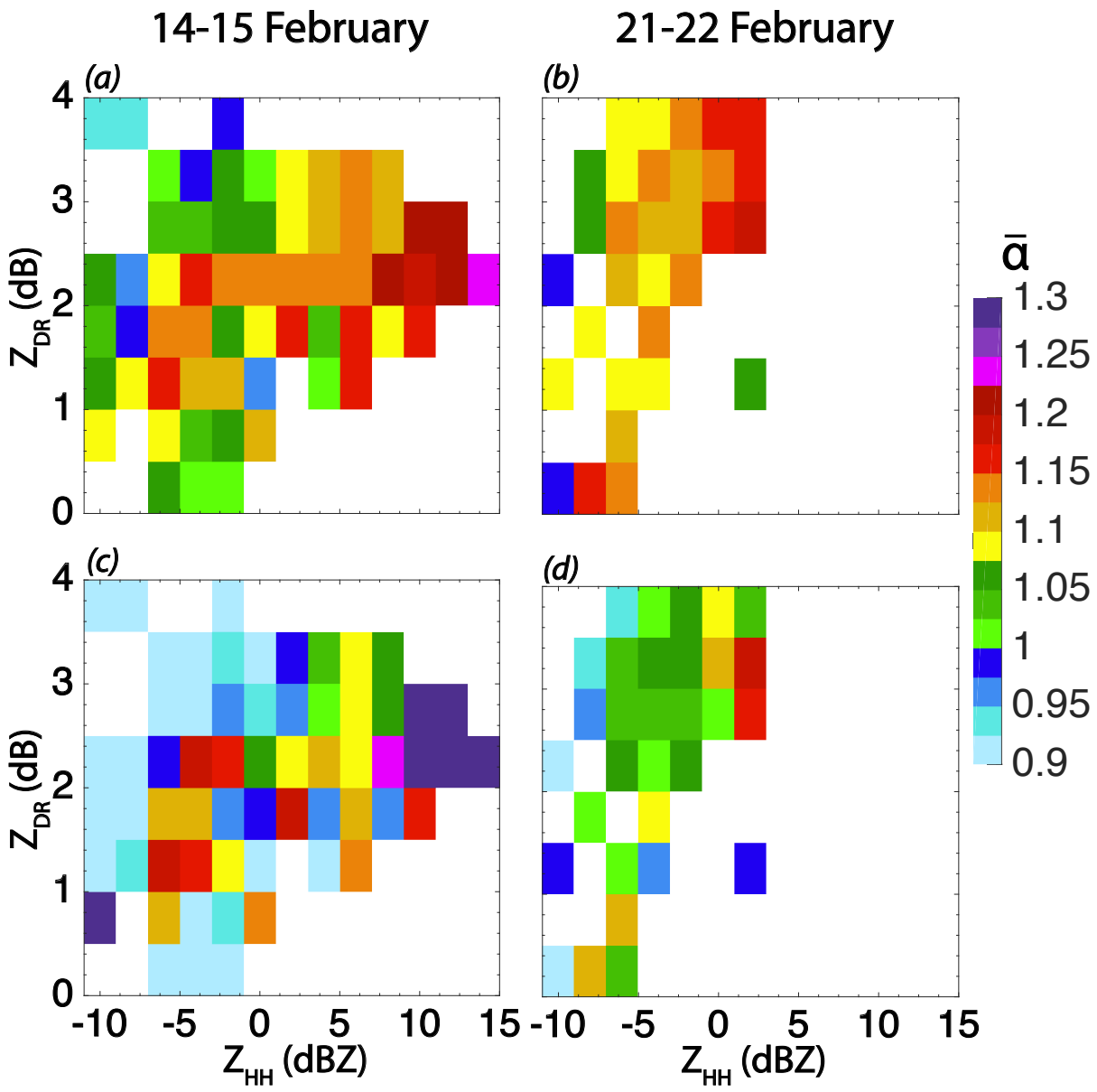

Figure 17: $\bar{\alpha}$ for particles coincident with radar measurements using (a,c) BL06 and (b,d) M02 at specific Z_{HH} and Z_{DR} binned intervals.

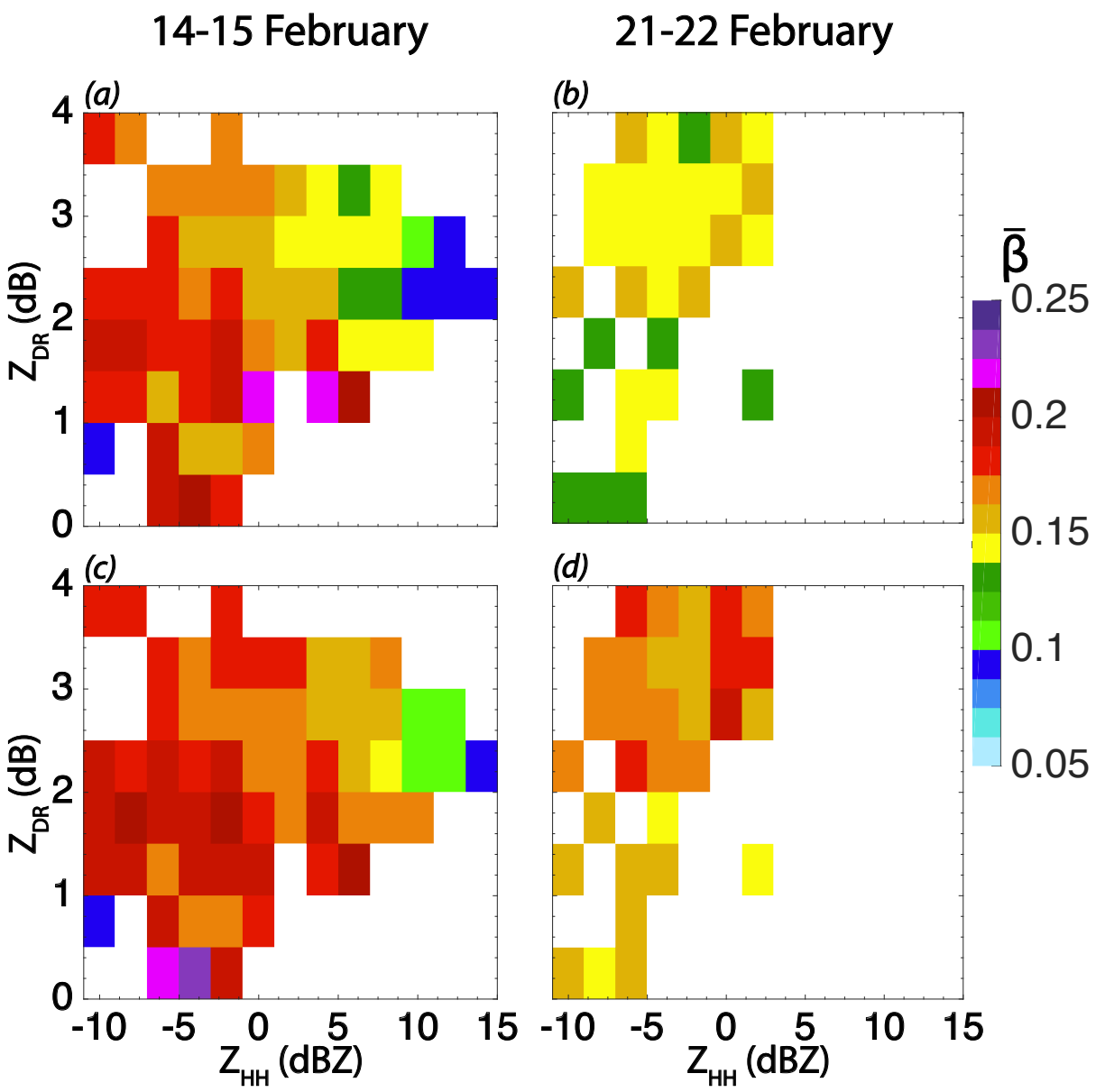

Figure 18: Same as in Fig. 17, but for $\bar{\beta}$.

References

Al-Sakka, H., A.-A. Boumahmoud, B. Fradon, S. J. Frasier, and P. Tabary, 2013: A New Fuzzy Logic Hydrometeor Classification Scheme Applied to the French X-, C-, and S-Band Polarimetric Radars. *Journal of Applied Meteorology and Climatology*, **52 (10)**, 2328–2344, doi:10.1175/JAMC-D-12-0236.1.

Aydin, K. and T. A. Seliga, 1984: Radar Polarimetric Backscattering Properties of Conical Graupel. *J. Atmos. Sci.*, **41 (11)**, 1887–1892, doi:10.1175/1520-0469(1984)041⟨1887:RPBPOC⟩2.0.CO;2.

Aydin, K., T. A. Seliga, and V. Balaji, 1986: Remote Sensing of Hail with a Dual Linear Polarization Radar. *J. Clim. Appl. Meteorol.*, **25 (10)**, 1475–1484, doi:10.1175/1520-0450(1986)025⟨1475:RSOHWA⟩2.0.CO;2.

Baker, B. and R. P. Lawson, 2006: Improvement in Determination of Ice Water Content from Two-Dimensional Particle Imagery. Part I: Image-to-Mass Relationships. *Journal of Applied Meteorology and Climatology*, **45 (9)**, 1282–1290, doi:10.1175/JAM2398.1.

Bechini, R. and V. Chandrasekar, 2015: A Semisupervised Robust Hydrometeor Classification Method for Dual-Polarization Radar Applications. *J. Atmos. Ocean. Technol.*, **32 (1)**, 22–47, doi:10.1175/JTECH-D-14-00097.1.

Bringi, V. N. and V. Chandrasekar, 2001: *Polarimetric Doppler Weather Radar: Principles and Applications*. Cambridge University Press, 636 pp.

Bringi, V. N., V. Chandrasekar, N. Balakrishnan, and D. S. Zrnić, 1990: An Examination of Propagation Effects in Rainfall on Radar Measurements at Microwave Frequencies. *J. Atmos. Ocean. Technol.*, **7 (6)**, 829–840, doi:10.1175/1520-0426(1990)007⟨0829:AEOPEI⟩2.0.CO;2.

Bringi, V. N., T. D. Keenan, and V. Chandrasekar, 2001: Correcting C-band radar reflectivity and differential reflectivity data for rain attenuation: a self-consistent method with constraints. *Geosci. Remote Sensing, IEEE Trans.*, **39 (9)**, 1906–1915, doi:10.1109/36.951081.

Bringi, V. N., J. Vivekanandan, and J. D. Tuttle, 1986: Multiparameter Radar Measurements in Colorado Convective Storms. Part II: Hail Detection Studies. *J. Atmos. Sci.*, **43 (22)**, 2564–2577, doi:10.1175/1520-0469(1986)043⟨2564:MRMICC⟩2.0.CO;2.

Chandrasekar, V., S. Lim, and E. Gorgucci, 2006: Simulation of X-Band Rainfall Observations from S-Band Radar Data. *J. Atmos. Ocean. Technol.*, **23 (9)**, 1195–1205, doi:10.1175/JTECH1909.1.

Chang, W.-Y., J. Vivekanandan, and T.-C. Chen Wang, 2014: Estimation of X-Band Polarimetric Radar Attenuation and Measurement Uncertainty Using a Variational Method. *J. Appl. Meteorol. Climatol.*, **53 (4)**, 1099–1119, doi:10.1175/JAMC-D-13-0191.1.

Cohen, J., 1988: *Statistical power analysis for the behavioral sciences*, Vol. 2nd. 567 pp., doi:10.1234/12345678.

Delrieu, G., H. Andrieu, and J. D. Creutin, 2000: Quantification of Path-Integrated Attenuation for X- and C-Band Weather Radar Systems Operating in Mediterranean Heavy Rainfall. *J. Appl. Meteorol.*, **39 (6)**, 840–850, doi:10.1175/1520-0450(2000)039⟨0840:QOPIAF⟩2.0.CO;2.

Diederich, M., A. Ryzhkov, C. Simmer, P. Zhang, and S. Trömel, 2014a: Use of Specific Attenuation for Rainfall Measurement at X-Band Radar Wavelengths Part 1: Radar Calibration and Partial Beam Blockage Estimation. *J. Hydrometeorol.*, doi:10.1175/JHM-D-14-0066.1.

Diederich, M., A. Ryzhkov, C. Simmer, P. Zhang, and S. Trömel, 2014b: Use of Specific Attenuation for Rainfall Measurement at X-Band Radar Wavelengths Part 2:

Rainfall Estimates and Comparison with Rain Gauges. *J. Hydrometeorol.*, doi:10.1175/JHM-D-14-0067.1.

Dolan, B. and S. A. Rutledge, 2009: A Theory-Based Hydrometeor Identification Algorithm for X-Band Polarimetric Radars. *J. Atmos. Ocean. Technol.*, **26 (10)**, 2071–2088, doi:10.1175/2009JTECHA1208.1.

El-Magd, A., V. Chandrasekar, V. N. Bringi, and W. Strapp, 2000: Multiparameter radar and in situ aircraft observation of graupel and hail. *IEEE Trans. Geosci. Remote Sens.*, **38 (1 II)**, 570–578, doi:10.1109/36.823951.

Field, P. R., 1999: Aircraft Observations of Ice Crystal Evolution in an Altostratus Cloud. *J. Atmos. Sci.*, **56 (12)**, 1925–1941, doi:10.1175/1520-0469(1999)056⟨1925:AOOICE⟩2.0.CO;2.

Fujiyoshi, Y. and G. Wakahama, 1985: On Snow Particles Comprising an Aggregate. *J. Atmos. Sci.*, **42 (15)**, 1667–1674, doi:10.1175/1520-0469(1985)042⟨1667:OSPCAA⟩2.0.CO;2.

Gans, R., 1912: Über die Form ultramikroskopischer Goldteilchen. *Ann. Phys.*, **342 (5)**, 881–900, doi:10.1002/andp.19123420503.

Goddard, J. W. F., J. Tan, and M. Thurai, 1994: Technique for calibration of meteorological radars using differential phase. 166–167 pp., doi:10.1049/el:19940119.

Gorgucci, E. and V. Chandrasekar, 2005: Evaluation of Attenuation Correction Methodology for Dual-Polarization Radars: Application to X-Band Systems. *J. Atmos. Ocean. Technol.*, **22 (8)**, 1195–1206, doi:10.1175/JTECH1763.1.

Griffin, E. M., T. J. Schuur, A. V. Ryzhkov, H. D. Reeves, and J. C. Picca, 2014: A Polarimetric and Microphysical Investigation of the Northeast Blizzard of 89 February 2013. *Weather Forecast.*, **29 (6)**, 1271–1294, doi:10.1175/WAF-D-14-00056.1.

Hall, M. P., S. M. Cherry, and J. W. F. Goddard, 1980: Use of dual-polarisation radar to measure rainfall rates and distinguish rain from ice particles. *Rec. IEEE 1980 Int. Radar Conf.*, Institute of Electrical and Electronics Engineers, New York, NY.

Hall, M. P. M., J. W. F. Goddard, and S. M. Cherry, 1984: Identification of hydrometeors and other targets by dual-polarization radar. *Radio Sci.*, **19 (1)**, 132–140, doi:10.1029/RS019i001p00132.

Heymsfield, A. J. and D. Baumgardner, 1985: Summary of a workshop on processing 2D probe data. *Bull. Am. Meteorol. Soc.*, **66 (4)**, 437–440.

Hobbs, P. V., S. Chang, and J. D. Locatelli, 1974: The dimensions and aggregation of ice crystals in natural clouds. *J. Geophys. Res.*, **79 (15)**, 2199–2206, doi:10.1029/JC079i015p02199.

Hogan, R. J., L. Tian, P. R. a. Brown, C. D. Westbrook, A. J. Heymsfield, and J. D. Eastment, 2012: Radar Scattering from Ice Aggregates Using the Horizontally Aligned Oblate Spheroid Approximation. *Journal of Applied Meteorology and Climatology*, **51 (3)**, 655–671, doi:10.1175/JAMC-D-11-074.1.

Höller, H., M. Hagen, P. F. Meischner, V. N. Bringi, and J. Hubbert, 1994: Life Cycle and Precipitation Formation in a Hybrid-Type Hailstorm Revealed by Polarimetric and Doppler Radar Measurements. *Journal of the Atmospheric Sciences*, **51 (17)**, 2500–2522, doi:10.1175/1520-0469(1994)051⟨2500:LCAPFI⟩2.0.CO;2.

Holroyd, E. W., 1987: Some Techniques and Uses of 2D-C Habit Classification Software for Snow Particles. *J. Atmos. Ocean. Technol.*, **4 (3)**, 498–511, doi:10.1175/1520-0426(1987)004⟨0498:STAUOC⟩2.0.CO;2.

Jackson, R. C., G. M. McFarquhar, J. Stith, M. Beals, R. A. Shaw, J. Jensen, J. Fugal, and A. Korolev, 2014: An Assessment of the Impact of Antishattering Tips and Artifact

Removal Techniques on Cloud Ice Size Distributions Measured by the 2D Cloud Probe. *J. Atmos. Ocean. Technol.*, **31 (12)**, 2567–2590, doi:10.1175/JTECH-D-13-00239.1.

King, W. D., 1985: Air Flow and Particle Trajectories around Aircraft Fuselages. Part III: Extensions to Particles of Arbitrary Shape. *J. Atmos. Ocean. Technol.*, **2 (4)**, 539–547, doi:10.1175/1520-0426(1985)002⟨0539:AFAPTA⟩2.0.CO;2.

King, W. D., 1986: Air Flow and Particle Trajectories around Aircraft Fuselages. IV: Orientation of Ice Crystals. *J. Atmos. Ocean. Technol.*, **3 (3)**, 433–439, doi:10.1175/1520-0426(1986)003⟨0433:AFAPTA⟩2.0.CO;2.

Knupp, K. R., et al., 2013: Meteorological Overview of the Devastating 27 April 2011 Tornado Outbreak. *Bull. Am. Meteorol. Soc.*, **95 (7)**, 1041–1062, doi:10.1175/BAMS-D-11-00229.1.

Kollias, P., J. Rémillard, E. Luke, and W. Szyrmer, 2011: Cloud radar Doppler spectra in drizzling stratiform clouds: 1. Forward modeling and remote sensing applications. *J. Geophys. Res.*, **116 (D13)**, D13 201, doi:10.1029/2010JD015237.

Korolev, A. and G. Isaac, 2003: Roundness and Aspect Ratio of Particles in Ice Clouds. *J. Atmos. Sci.*, **60 (15)**, 1795–1808, doi:10.1175/1520-0469(2003)060⟨1795:RAAROP⟩2.0.CO;2.

Korolev, A., G. A. Isaac, and J. Hallett, 2000: Ice particle habits in stratiform clouds. *Q. J. R. Meteorol. Soc.*, **126 (569)**, 2873–2902, doi:10.1002/qj.49712656913.

Korolev, A., A. Shashkov, and H. Barker, 2014: Calibrations and Performance of the Airborne Cloud Extinction Probe. *J. Atmos. Ocean. Technol.*, **31 (2)**, 326–345, doi:10.1175/JTECH-D-13-00020.1.

Korolev, A. V., E. F. Emery, J. W. Strapp, S. G. Cober, G. A. Isaac, M. Wasey, and D. Marcotte, 2011: Small Ice Particles in Tropospheric Clouds: Fact or Artifact? Airborne

Icing Instrumentation Evaluation Experiment. *Bull. Am. Meteorol. Soc.*, **92 (8)**, 967–973, doi:10.1175/2010BAMS3141.1.

Korolev, A. V., G. A. Isaac, and J. Hallett, 1999: Ice particle habits in Arctic clouds. *Geophys. Res. Lett.*, **26 (9)**, 1299–1302, doi:10.1029/1999GL900232.

Lim, S., V. Chandrasekar, and V. Bringi, 2005: Hydrometeor classification system using dual-polarization radar measurements: model improvements and in situ verification. *IEEE Transactions on Geoscience and Remote Sensing*, **43 (4)**, 792–801, doi:10.1109/TGRS.2004.843077.

Lim, S., R. Cifelli, V. Chandrasekar, and S. Y. Matrosov, 2013: Precipitation Classification and Quantification Using X-Band Dual-Polarization Weather Radar: Application in the Hydrometeorology Testbed. *Journal of Atmospheric and Oceanic Technology*, **30 (9)**, 2108–2120, doi:10.1175/JTECH-D-12-00123.1.

Liu, H. and V. Chandrasekar, 2000: Classification of Hydrometeors Based on Polarimetric Radar Measurements: Development of Fuzzy Logic and Neuro-Fuzzy Systems, and In Situ Verification. *Journal of Atmospheric and Oceanic Technology*, **17 (2)**, 140–164, doi:10.1175/1520-0426(2000)017⟨0140:COHBOP⟩2.0.CO;2.

Magono, C., 1954: On the Falling Velocity of Solid Precipitation Elements. *Sci. Reports Yokohama Natl. Univ.*, **13 (33)**.

McFarquhar, G. M., M. S. Timlin, T. Nousiainen, and P. Yang, 2005: A New Representation of the Single-Scattering Properties for Mid-latitude Clouds and its Impacts. *Fifteenth ARM Sci. Team Meet. Proc.*, Daytona Beach, FL.

McFarquhar, G. M., P. Yang, A. Macke, and A. J. Baran, 2002: A New Parameterization of Single Scattering Solar Radiative Properties for Tropical Anvils Using Observed Ice Crystal Size and Shape Distributions. *J. Atmos. Sci.*, **59 (16)**, 2458–2478, doi:10.1175/1520-0469(2002)059⟨2458:ANPOSS⟩2.0.CO;2.

Mullins, S. and K. R. Knupp, 2009: Observations of hurricane Ike (2008) from the Mobile Alabama X-band radar. *34th Conf. Radar Meteorol.*, American Meteorological Society, Williamsburg, VA.

Oue, M., M. R. Kumjian, Y. Lu, Z. Jiang, E. E. Clothiaux, J. Verlinde, and K. Aydin, 2015: X-Band Polarimetric and Ka-Band Doppler Spectral Radar Observations of a Graupel-Producing Arctic Mixed-Phase Cloud. *J. Appl. Meteorol. Climatol.*, **54 (6)**, 1335–1351, doi:10.1175/JAMC-D-14-0315.1.

Park, H. S., A. V. Ryzhkov, D. S. Zrnić, and K.-E. Kim, 2009: The Hydrometeor Classification Algorithm for the Polarimetric WSR-88D: Description and Application to an MCS. *Weather and Forecasting*, **24 (3)**, 730–748, doi:10.1175/2008WAF2222205.1.

Park, S.-G., V. N. Bringi, V. Chandrasekar, M. Maki, and K. Iwanami, 2005a: Correction of Radar Reflectivity and Differential Reflectivity for Rain Attenuation at X Band. Part I: Theoretical and Empirical Basis. *Journal of Atmospheric and Oceanic Technology*, **22 (11)**, 1621–1632, doi:10.1175/JTECH1803.1.

Picca, J. C., D. M. Schultz, B. A. Colle, S. Ganetis, D. R. Novak, and M. J. Sienkiewicz, 2014: The Value of Dual-Polarization Radar in Diagnosing the Complex Microphysical Evolution of an Intense Snowband. *Bull. Am. Meteorol. Soc.*, **95 (12)**, 1825–1834, doi:10.1175/BAMS-D-13-00258.1.

Plummer, D. M., S. Göke, R. M. Rauber, and L. Di Girolamo, 2010: Discrimination of Mixed- versus Ice-Phase Clouds Using Dual-Polarization Radar with Application to Detection of Aircraft Icing Regions*. *Journal of Applied Meteorology and Climatology*, **49 (5)**, 920–936, doi:10.1175/2009JAMC2267.1.

Plummer, D. M., G. M. McFarquhar, R. M. Rauber, B. F. Jewett, and D. C. Leon, 2014: Structure and Statistical Analysis of the Microphysical Properties of Generating Cells

in the Comma Head Region of Continental Winter Cyclones. *J. Atmos. Sci.*, **71 (11)**, 4181–4203, doi:10.1175/JAS-D-14-0100.1.

Plummer, D. M., G. M. McFarquhar, R. M. Rauber, B. F. Jewett, and D. C. Leon, 2015: Microphysical Properties of Convectively Generated Fall Streaks within the Stratiform Comma Head Region of Continental Winter Cyclones. *J. Atmos. Sci.*, **72 (6)**, 2465–2483, doi:10.1175/JAS-D-14-0354.1, URL `http://dx.doi.org/10.1175/JAS-D-14-0354.1`.

Rauber, R. M., et al., 2014: Stability and Charging Characteristics of the Comma Head Region of Continental Winter Cyclones. *J. Atmos. Sci.*, **71 (5)**, 1559–1582, doi:10.1175/JAS-D-13-0253.1.

Rosenow, A. A., D. M. Plummer, R. M. Rauber, G. M. McFarquhar, B. F. Jewett, and D. Leon, 2014: Vertical Velocity and Physical Structure of Generating Cells and Convection in the Comma Head Region of Continental Winter Cyclones. *J. Atmos. Sci.*, **71 (5)**, 1538–1558, doi:10.1175/JAS-D-13-0249.1.

Ryzhkov, A., M. Diederich, P. Zhang, and C. Simmer, 2014: Potential Utilization of Specific Attenuation for Rainfall Estimation, Mitigation of Partial Beam Blockage, and Radar Networking. *J. Atmos. Ocean. Technol.*, **31 (3)**, 599–619, doi:10.1175/JTECH-D-13-00038.1.

Ryzhkov, A. V., T. J. Schuur, D. W. Burgess, P. L. Heinselman, S. E. Giangrande, and D. S. Zrnic, 2005: The Joint Polarization Experiment: Polarimetric Rainfall Measurements and Hydrometeor Classification. *Bull. Am. Meteorol. Soc.*, **86 (6)**, 809–824, doi:10.1175/BAMS-86-6-809.

Schuur, T. J., H.-S. Park, A. V. Ryzhkov, and H. D. Reeves, 2012: Classification of Precipitation Types during Transitional Winter Weather Using the RUC Model and Polarimetric Radar Retrievals. *Journal of Applied Meteorology and Climatology*, **51 (4)**, 763–779.

Seliga, T. A. and V. N. Bringi, 1976: Potential Use of Radar Differential Reflectivity Mea-

surements at Orthogonal Polarizations for Measuring Precipitation. *Journal of Applied Meteorology*, **15 (1)**, 69–76, doi:10.1175/1520-0450(1976)015⟨0069:PUORDR⟩2.0.CO;2.

Snyder, J. C., H. B. Bluestein, G. Zhang, and S. J. Frasier, 2010: Attenuation Correction and Hydrometeor Classification of High-Resolution, X-band, Dual-Polarized Mobile Radar Measurements in Severe Convective Storms. *J. Atmos. Ocean. Technol.*, **27 (12)**, 1979–2001, doi:10.1175/2010JTECHA1356.1.

Stoelinga, M. T., J. D. Locatelli, and C. P. Woods, 2007: The Occurrence of Irregular Ice Particles in Stratiform Clouds. *J. Atmos. Sci.*, **64 (7)**, 2740–2750, doi:10.1175/JAS3962.1.

Straka, J. M. and D. S. Zrnić, 1993: An algorithm to deduce hydrometeor types and contents from multi-parameter radar data. *26th Conference on Radar Meteorology*, American Meteorological Society, Boston, MA, 513–515.

Tang, L., J. Zhang, and Y. Wang, 2013: Uncertainty Analyses of the Operational WSR-88D Hydrometeor Classification Project. *36th Conf. Radar Meteorol.*, American Meteorological Society, Breckenridge, CO.

Testud, J., E. Le Bouar, E. Obligis, and M. Ali-Mehenni, 2000: The Rain Profiling Algorithm Applied to Polarimetric Weather Radar. *J. Atmos. Ocean. Technol.*, **17 (3)**, 332–356, doi:10.1175/1520-0426(2000)017⟨0332:TRPAAT⟩2.0.CO;2.

Thompson, E. J., S. A. Rutledge, B. Dolan, V. Chandrasekar, and B. L. Cheong, 2014: A Dual-Polarization Radar Hydrometeor Classification Algorithm for Winter Precipitation. *Journal of Atmospheric and Oceanic Technology*, **31 (7)**, 1457–1481, doi:10.1175/JTECH-D-13-00119.1.

Tyynelä, J., J. Leinonen, D. Moisseev, and T. Nousiainen, 2011: Radar Backscattering from Snowflakes: Comparison of Fractal, Aggregate, and Soft Spheroid Models. *J. Atmos. Ocean. Technol.*, **28 (11)**, 1365–1372, doi:10.1175/JTECH-D-11-00004.1.

Vivekanandan, J., S. M. Ellis, R. Oye, D. S. Zrnic, a. V. Ryzhkov, and J. Straka, 1999: Cloud Microphysics Retrieval Using S-band Dual-Polarization Radar Measurements. *Bulletin of the American Meteorological Society*, **80 (3)**, 381–388, doi:10.1175/1520-0477(1999)080⟨0381:CMRUSB⟩2.0.CO;2.

Wen, G., A. Protat, P. T. May, X. Wang, and W. Moran, 2015: A Cluster-Based Method for Hydrometeor Classification Using Polarimetric Variables. Part I: Interpretation and Analysis. *J. Atmos. Ocean. Technol.*, **32 (7)**, 1320–1340, doi:10.1175/JTECH-D-13-00178.1.

Wolde, M., D. Hudak, B. Currie, S. G. Cober, P. Rodriguez, I. Zawadzki, G. A. Isaac, and D. Marcotte, 2003: Radar Signatures of Winter Clouds from Aircraft In-Situ Data and Ground-Based Radar Observations. *31st Int. Conf. Radar Meteorol.*, American Meteorological Society, Seattle, WA, 973–975.

Zong, R., L. Liu, and Y. Yin, 2013: Relationship between cloud characteristics and radar reflectivity based on aircraft and cloud radar co-observations. *Adv. Atmos. Sci.*, **30 (5)**, 1275–1286, doi:10.1007/s00376-013-2090-7.

Zrnić, D. S., A. Ryzhkov, J. Straka, Y. Liu, and J. Vivekanandan, 2001: Testing a Procedure for Automatic Classification of Hydrometeor Types. *Journal of Atmospheric and Oceanic Technology*, **18 (6)**, 892–913, doi:10.1175/1520-0426(2001)018⟨0892:TAPFAC⟩2.0.CO;2.

Zrnić, D. S., A. V. Ryzhkov, J. M. Straka, Y. Liu, and J. Vivekanandan, 2000: Sensitivity of an automatic procedure for hydrometeor classification. *Geoscience and Remote Sensing Symposium, 2000. Proceedings. IGARSS 2000. IEEE 2000 International*, IEEE, Vol. 4, 1574–1576 vol.4, doi:10.1109/IGARSS.2000.857276.